Journal of Fluids and Structures 136 (2025) 104327

Contents lists available at ScienceDirect

Journal of Fluids and Structures

journal homepage: www.elsevier.com/locate/yjfls

Steady-state nonlinear dynamics of a flexible beam with large deformation under oscillatory flow

Jingkun Gao [a], Weidong Zhu [a,*], Yaqing Jin [b], Pengyao Gong [b]

[a] Department of Mechanical Engineering, University of Maryland, Baltimore County, 1000 Hilltop Circle, Baltimore, MD, 21250, USA
[b] Department of Mechanical Engineering, University of Texas at Dallas, Richardson, Texas, 75080, USA

ARTICLE INFO

Keywords:
Nonlinear dynamics
Fluid-solid coupling
Large deformation beams

ABSTRACT

This work investigates the steady-state nonlinear dynamics of a large-deformation flexible beam model under oscillatory flow. A flexible beam dynamics model combined with hydrodynamic loading is employed using large deformation beam theory. The equations of motion discretised using the high-order finite element method (FEM) are solved in the time domain using the efficient Galerkin averaging-incremental harmonic balance (EGA-IHB) method. The arc-length continuation method and Hsu's method trace stable and unstable solutions. The numerical results are in accordance with the physical experimental results and reveal multiple resonance phenomena. Low-order resonances exhibit hardening due to geometric nonlinearity, while higher-order resonances transition from softening to hardening influenced by inertia and geometric nonlinearity. A strong coupling between tensile and bending deformation is observed. The axial deformation is dominated by inertia, while bending resonance is influenced by an interplay between inertia, structure stiffness, and fluid drag. Finally, the effects of two dimensionless parameters, Keulegan and Carpenter number (KC) and Cauchy number (Ca), on the response of the flexible beam are discussed.

1. Introduction

The work of flexible structures submerged in fluids has been the subject of considerable research activity in recent years, reflecting their potential for a wide range of applications in fields as diverse as bio-inspired machinery with soft bodies (Xia et al., 2023; Li et al., 2021, 2024), renewable energy harvesting via flow-induced vibrations of piezoelectric materials (Mazharmanesh et al., 2022; Akcabay and Young, 2012; Chatterjee et al., 2024), fluid-conveying pipeline (Farokhi et al., 2021; Dehrouyeh-Semnani, 2025; Guo et al., 2024), and underwater ecological protection (Poi et al., 2021; Vymazal, 2013). Among the various flexible structures, flexible beam-like structures frequently display intricate dynamical behaviours due to their substantial disparities in normal and axial stiffnesses. These structures are susceptible to considerable elastic deformations, particularly in environments characterised by oscillatory flow induced by waves (Wang et al., 2022). The interaction of flexible beam-like structures with fluids represents a typical and important object of study, with aquatic plants (de Langre, 2019) representing a specific example. These plants are pivotal in aquatic ecosystems, providing habitats, sustenance and oxygen for marine organisms. Additionally, they can effectively safeguard coastal regions and communities from erosion by attenuating wave energy (Henderson, 2019). The theoretical modelling of the dynamics of flexible beam-like structures in oscillatory flows is fundamental to understanding the interaction between the fluid and the aquatic plants due

* Corresponding author.
E-mail address: wzhu@umbc.edu (W. Zhu).

https://doi.org/10.1016/j.jfluidstructs.2025.104327
Received 19 November 2024; Received in revised form 5 April 2025; Accepted 21 April 2025
Available online 2 May 2025

to their high degree of flexibility and consequent 'reconfiguration' (Vogel, 1984), which results in significant relative motions between the fluid and the aquatic plants.

Although Fluid-Structure Interaction (FSI) models (Jin and Zhang, 2022; Wei et al., 2024) are the most effective way to capture fluid-solid interactions, and considerable research effort has been devoted to developing computational hydrodynamics models for flexible elongated structures in recent years (Divyaprakash, 2024; Huang et al., 2007; Chen et al., 2024), their high computational cost makes them unsuitable for large-scale parametric studies.

Consequently, many studies have utilised simplified modelling approaches, particularly when specific assumptions can reasonably simplify the fluid motion. In the case of oscillatory flows, the velocity at any given point within the flow field is a function of time. While the actual flow velocity variation can be highly complex, theoretical studies often assume that the flow velocity is dominated by a single frequency component (Zhang and Nakamura, 2024; Jacobsen et al., 2019). This assumption enables the differentiation of various oscillatory flow conditions by identifying two key parameters: the maximum flow velocity and the frequency of flow velocity fluctuations. For a specific oscillatory flow scenario, the movement of the flexible beam within the flow field will gradually reach a stable equilibrium state. Investigating this steady-state periodic response is of particular significance for elucidating the amplitude-frequency characteristics of the flexible beam structure.

Given that the flow velocity has been predetermined, the hydrodynamic forces are regarded as non-conservative loads related to the attitude of the flexible beam. This results in the driving of a rigid beam connected by torsion springs in series (Zeller et al., 2014) or a non-extensible cantilevered flexible beam (Luhar and Nepf, 2011, 2016) for a wide range of motions. The specific state of motion of the flexible beam under different oscillatory flow conditions results from the combined effect of the hydrodynamic forces and the structural elastic restoring forces on the flexible beam, given the finite structural stiffness of the beam itself (J. Lei and Nepf, 2019). The introduction of structural stiffness in flexible beams also allows for further refinement of modelling, for example, by considering differences between aquatic plant stems and leaves (Zhang and Nepf, 2021; Marjoribanks and Paul, 2022), by considering both the pure flow component in oscillatory flow (Beth Schaefer and Nepf, 2022) or by partially surfacing the water (Yin et al., 2023b). This, in turn, results in notable discrepancies between the hydrodynamics and those obtained from rigid-body models (Cavallaro et al., 2018; Reis et al., 2024), which in turn affects the quantitative assessment of the efficiency of wave attenuation of aquatic plants (Mullarney and Henderson, 2010; J. Lei and Nepf, 2019; Yin et al., 2023a).

Nevertheless, few studies have investigated the resonance phenomenon of flexible beams excited by oscillatory flows with a specific frequency of flow velocity change. Leclercq and de Langre (2018) investigated the 'reconfiguration' of two-dimensional flexible beams in oscillatory flows. The authors identify four distinct states of motion for the flexible beam, contingent upon the offset of the fluid particles relative to the beam dimensions and the frequency of flow oscillations about the beam eigenfrequency. When the fluid amplitude is smaller than the width of the structure, the fluid inertia exceeds the drag force, triggering a resonance phenomenon in the flexible beam. This phenomenon leads to an amplification of the internal stresses. Kumar et al. (2021) conducted a theoretical analysis demonstrating that the resonance phenomenon only occurs in states of motion dominated by inertia. This contrasts states of motion, which are dominated by the additional inertia, such as that of the fluid. This suggests that resonance does not occur in drag-dominated motions. However, their model is based on the assumption of small deformations. Hasan et al. (2023) specifically investigated the effect of geometric nonlinearities on the amplitude-frequency characteristics due to the extensive range of motion of the flexible beam. They observed both stiffening effects due to geometric nonlinearities and instability due to bifurcation. Notwithstanding the comprehensive analysis of the wide range of motion of the flexible beam, the additional inertial forces of the fluid have been disregarded in the investigation.

In the modelling of cantilevered flexible beams, the tensile deformation was disregarded in most models employed in the previous study. Given that the axial stiffness of a flexible beam is typically considerably more significant than its bending stiffness, the load frequency required to excite the low-order bending resonance is significantly less than that needed to excite the tensile resonance in terms of the intrinsic vibration mode of the flexible beam itself. Nevertheless, due to the intricate impact of oscillating flow on the flexible beam, the possibility of tensile resonance also exists at low frequencies.

Furthermore, a comprehensive parametric investigation is imperative to elucidate the dynamic response of the flexible beam fully. However, due to the complexity of nonlinear coupling effects, conventional numerical methods encounter significant challenges in terms of computational efficiency. To achieve this, this work employs the incremental harmonic balance (IHB) method (LaBryer and Attar, 2010; Hall et al., 2013; Yan et al., 2023), an efficient numerical technique, as the principal instrument for investigating the steady-state response. The IHB method demonstrates remarkable computational efficiency in addressing intricate nonlinear systems, effectively reducing computational time without compromising accuracy. Consequently, this work addresses the modelling of the nonlinear dynamics of flexible beams. It guarantees the implementation of an efficient numerical simulation and analysis over a comprehensive range of parameter spaces by utilising the IHB method.

Although considerable progress has been made in the study of flexible beams in oscillatory flows based on equivalent fluid force models, it is worth noting that these studies require further simplification of the models. While these simplifications reduce computational complexity in some cases, they do not fully explain the dynamics of flexible beams under large deformation conditions. Moreover, they are particularly limited in their ability to analyse resonance and instability phenomena. In light of these limitations, this work aims to comprehensively analyse the resonance characteristics and potential instability behaviour of flexible beams in oscillatory flows by avoiding simplifying assumptions on tensile deformations and fully accounting for hydrodynamic and geometric nonlinear effects. Furthermore, the efficient solution of steady-state dynamics for flexible beams in oscillating flows and the discrimination of stability is achieved by high-order FEM, IHB method, and Floquet theory with guaranteed accuracy.

The following is a description of the structure of this work. Section 2 commences with underwater flexible beam dynamics modelling, employing the tenets of large deformation beam theory and equivalent hydrodynamics. The equations of motion are

established based on the high-order FEM. The EGA-IHB method obtains the steady-state periodic solution and tracks the solution branching, utilising the arc length extension and Hsu's methods. Section 3 presents the findings of a physical experiment on an underwater flexible beam, compared to the numerical modelling results. Section 4 examines the nonlinear steady-state dynamics of an underwater flexible beam subjected to oscillating flow, analysing its amplitude-frequency characteristic curves, specific kinematic states and forces. In conclusion, Section 5 presents the findings of this work and offers suggestions for further research.

2. Numerical method

In this work, a flexible beam dynamics model is employed in conjunction with an equivalent hydrodynamic loading model to examine the nonlinear steady-state dynamics of an underwater flexible beam subjected to wave action. This work employs a combination of flexible beam dynamics and hydrodynamics, utilising large deformation beam theory and equivalent fluid forces to simulate the oscillatory behaviour of the flexible beam in the submerged state. The empirical coefficients in the equivalent fluid forces are derived from existing physical experiments to ensure an accurate modelling of the hydrodynamics.

The governing equations of motion are strongly nonlinear partial differential equations, which are spatially discretised using the high-order FEM. The temporal discretization is performed using the EGA-IHB method, which is particularly effective for analysing steady-state dynamics in nonlinear systems due to its computational efficiency, which is significantly superior to that of conventional time domain methods. The arc-length continuation and Hsu's methods are employed to investigate the response of the flexible beam under hydrodynamic conditions. This approach enables the solution curve to be traced continuously, thus facilitating the identification of stable and unstable equilibrium states.

2.1. Underwater flexible beam dynamics model based on high-order FEM

A dynamical model, which accurately describes the geometrical configuration of the flexible beam, was developed by Li (2015). The following assumptions underpin this model:

1) The underwater flexible beam is composed of homogeneous and isotropic materials. Its cross-section, perpendicular to its centroidal axis, retains its planar configuration following deformation.
2) While elongation along the centroidal axis of the flexible beam is accounted for, the area of any cross-section remains constant following deformation.
3) It is assumed that the deformation of the beam occurs only in the OXY plane and that during deformation, the cross-section rotates only about the axis perpendicular to the OXY plane but not about the X-axis and the Y-axis.

Consider the motion of a flexible beam aligned with linear gravity waves on the surface of a water layer with a mean depth H and density ρ_f, as illustrated in Fig. 1. The physical parameters of the beam are as follows: length l, mass density ρ, Young's modulus E, width b, thickness h, cross-sectional area $A = hb$, and area moment of inertia $I = bh^3/12$. The position of a cross-section along the beam can be described by the unstretched arc-length coordinate s along the centroidal axis, where $0 \le s \le l$. The Cartesian coordinates of a point P on the centroidal line of the beam, before and after deformation, are given by $\mathbf{r}(s) = (s, 0)$ and $\mathbf{R}(s,t) = (s + u_x, u_y)$ in the OXY coordinate system, respectively. Here, $u_x(s,t)$ and $u_y(s,t)$ represent the longitudinal and transverse deformations of the point P, respectively. The stretch strain $\varepsilon(s,t)$ and slope angle $\varphi(s,t)$ are employed to describe the deformation of the planar beam. Thus, the displacement vector $\mathbf{u}(s,t) = \begin{pmatrix} u_x & u_y \end{pmatrix}^T$ at the point P can be expressed,

$$\mathbf{u} = \begin{pmatrix} \int_0^s (e\cos\varphi - 1)\mathrm{d}\zeta \\ \int_0^s (e\sin\varphi)\mathrm{d}\zeta \end{pmatrix} \tag{1}$$

where, $e = \varepsilon + 1$ denotes axial elongation.

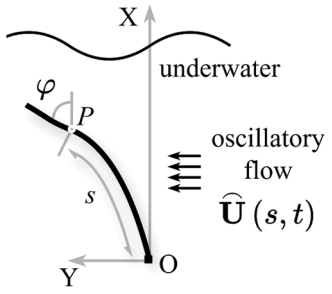

Fig. 1. Underwater flexible beam model.

In the FEM, the flexible beam is divided into N^e+1 discrete nodes, with the arc length coordinate of the ith node denoted as s_i, $i=0,\cdots,N^e$. Each pair of adjacent nodes forms an element, and the local coordinate within the element is defined as $\bar{s}=(s-s_i)/l_i$, where $l_i=s_{i+1}-s_i$. By using interpolation functions to discretise $\varepsilon(s,t)$ and $\varphi(s,t)$ in the spatial domain, the quantities $\varepsilon^{e,i}(\bar{s},t)$ and $\varphi^{e,i}(\bar{s},t)$ within the ith element are obtained,

$$\begin{cases}\varepsilon^{e,i}=\mathbf{N}_1^i\cdot\mathbf{d}^{(n)}\\ \varphi^{e,i}=\mathbf{N}_2^i\cdot\mathbf{d}^{(n)}\end{cases} \tag{2}$$

where, $\mathbf{d}^{(n)}(t)=\begin{pmatrix}\varepsilon^0 & \varphi^0 & \kappa^0 & \cdots & \varepsilon^i & \varphi^i & \kappa^i & \cdots & \varepsilon^n & \varphi^n & \kappa^n\end{pmatrix}^T$ denotes the total degrees of freedom vector, where $\varepsilon^i=\varepsilon(s_i,t)$, $\varphi^i=\varphi(s_i,t)$, and $\kappa^i=\partial\varphi/\partial s(s_i,t)$; $\mathbf{N}_1^i(\bar{s})$ denotes the linear interpolation function for the ith beam element; $\mathbf{N}_2^i(\bar{s})$ denotes the Hermite interpolation function for the ith beam element. Thus, the displacement vector at s can be expressed as

$$\mathbf{u}(s,t)=\begin{pmatrix}\sum_{j=1}^{i-1}\int_{s_{j-1}}^{s_j}\left(e^{e,i}C_\varphi^{e,i}-1\right)\mathrm{d}\zeta+\int_{s_{i-1}}^{s}\left(e^{e,i}C_\varphi^{e,i}-1\right)\mathrm{d}\zeta\\ \sum_{j=1}^{i-1}\int_{s_{j-1}}^{s_j}\left(e^{e,i}S_\varphi^{e,i}\right)\mathrm{d}\zeta+\int_{s_{i-1}}^{s}\left(e^{e,i}S_\varphi^{e,i}\right)\mathrm{d}\zeta\end{pmatrix},\ s_{i-1}\le s\le s_i,\ i=1,2,\ldots N^e \tag{3}$$

where, $C_\varphi^{e,i}=\cos\varphi^{e,i}$; $S_\varphi^{e,i}=\sin\varphi^{e,i}$. Define the operator,

$$\mathrm{I}[\bullet]=\sum_{j=1}^{i-1}\int_{s_{j-1}}^{s_j}(\bullet)\mathrm{d}\zeta+\int_{s_{i-1}}^{s}(\bullet)\mathrm{d}\zeta \tag{4}$$

Application of the Hamilton's principle (Meirovitch, 2010), the governing equations of the flexible beam can be obtained,

$$\mathbf{M}\cdot\frac{\mathrm{d}^2\mathbf{d}^{(n)}}{\mathrm{d}t^2}=\mathbf{Q} \tag{5}$$

where, $\mathbf{M}(\mathbf{d}^{(n)},t)=\sum_{k=1}^{N^e}\int_0^1\mathbf{M}^{e,i}\mathrm{d}\bar{s}$ denotes the mass matrix and the element mass matrix $\mathbf{M}^{e,i}$ is given by,

$$\mathbf{M}^{e,i}=\rho A\left(\mathbf{M}_x^{e,i^T}\cdot\mathbf{M}_x^{e,i}+\mathbf{M}_y^{e,i^T}\cdot\mathbf{M}_y^{e,i}\right) \tag{6}$$

where $\mathbf{M}_x^{e,i}=\mathrm{I}\left[\mathbf{N}_1^iC_\varphi^{e,i}-\mathbf{N}_2^ie^{e,i}S_\varphi^{e,i}\right]$ and $\mathbf{M}_y^{e,i}=\mathrm{I}\left[\mathbf{N}_1^jS_\varphi^{e,j}+\mathbf{N}_2^je^{e,i}C_\varphi^{e,j}\right]$.

$\mathbf{Q}\left(\mathbf{d}^{(n)},\mathrm{d}\mathbf{d}^{(n)}/\mathrm{d}t,\mathrm{d}^2\mathbf{d}^{(n)}/\mathrm{d}t^2,t\right)=\sum_{k=1}^{N^e}\int_0^1\left(\mathbf{Q}_F^{e,i}-\mathbf{Q}_I^{e,i}-\mathbf{Q}_E^{e,i}-\mathbf{Q}_C^i\right)\mathrm{d}\bar{s}$ denotes the generalised force vector, and the element generalized force vectors are respectively given by,

$$\mathbf{Q}_F^{e,i}=\mathbf{M}_x^{e,i^T}\cdot F_x^{e,i}+\mathbf{M}_y^{e,i^T}\cdot F_y^{e,i} \tag{7}$$

$$\mathbf{Q}_I^{e,i}=\rho A\begin{pmatrix}\mathrm{I}\left[-2\frac{\partial\varepsilon^{e,i}}{\partial t}\frac{\partial\varphi^{e,i}}{\partial t}S_\varphi^{e,i}-\left(\frac{\partial\varphi^{e,i}}{\partial t}\right)^2e^{e,i}C_\varphi^{e,i}\right]\mathbf{M}_x^{e,i^T}\\ +\mathrm{I}\left[2\frac{\partial\varepsilon^{e,i}}{\partial t}\frac{\partial\varphi^{e,i}}{\partial t}C_\varphi^{e,i}-\left(\frac{\partial\varphi^{e,i}}{\partial t}\right)^2e^{e,i}S_\varphi^{e,i}\right]\mathbf{M}_y^{e,i^T}\end{pmatrix} \tag{8}$$

$$\mathbf{Q}_E^{e,i}=\left(EA\mathbf{N}_1^{i^T}\cdot\mathbf{N}_1^i+EI\frac{\partial\mathbf{N}_2^{i^T}}{\partial\bar{s}}\cdot\frac{\partial\mathbf{N}_2^i}{\partial\bar{s}}\right)\cdot\mathbf{d}^{(n)} \tag{9}$$

Table 1
Equivalent fluid force.

Buoyancy force	$\mathbf{F}_B=\begin{pmatrix}(\rho-\rho_f)gbh & 0\end{pmatrix}^T$
Drag force	$\mathbf{F}_D=\frac{1}{2}\rho bC_D\lvert U_t\rvert U_t\mathbf{T}_t$
Skin friction force	$\mathbf{F}_F=\frac{1}{2}\rho bC_F\lvert U_n\rvert U_n\mathbf{T}_n$
Froude-Krylov force	$\mathbf{F}_{VB}=\rho bh\widehat{\mathbf{U}}$
Added inertial force	$\mathbf{F}_{AM}=\frac{\pi}{4}\rho_fb^2C_M\left(\frac{\partial\widehat{\mathbf{U}}}{\partial t}-\frac{\partial^2\mathbf{u}}{\partial t^2}\right)$

$$\mathbf{Q}_C^{e,i} = \alpha\left(EA\mathbf{N}_1^{i\,T}\cdot\mathbf{N}_1^i + EI\frac{\partial\mathbf{N}_2^{i\,T}}{\partial\bar{s}}\cdot\frac{\partial\mathbf{N}_2^i}{\partial\bar{s}}\right)\cdot\frac{\partial\mathbf{d}^{(n)}}{\partial t} \tag{10}$$

where, α denotes the material damping factor;

$\mathbf{F}^{e,i}\left(\mathbf{d}^{(n)}, \mathrm{d}\mathbf{d}^{(n)}/\mathrm{d}t, \mathrm{d}^2\mathbf{d}^{(n)}/\mathrm{d}t^2, t\right) = \begin{pmatrix} F_x^{e,i} & F_y^{e,i}\end{pmatrix}^T = \mathbf{F}_B^{e,i} + \mathbf{F}_D^{e,i} + \mathbf{F}_F^{e,i} + \mathbf{F}_{VB}^{e,i} + \mathbf{F}_{AM}^{e,i}$ denotes the equivalent fluid force vector acting on the ith element. The equivalent fluid force includes net buoyancy force $\mathbf{F}_B^{e,i} = \mathbf{F}_B(s_i, t)$ which is defined as the combined effects of gravity and water buoyancy, drag force $\mathbf{F}_D^{e,i} = \mathbf{F}_D(s_i, t)$, skin friction force $\mathbf{F}_F^{e,i} = \mathbf{F}_F(s_i, t)$, Froude-Krylov force $\mathbf{F}_{VB}^{e,i} = \mathbf{F}_{VB}(s_i, t)$ which arises from the unsteady pressure gradient (Batchelor, 1999), and added inertial force $\mathbf{F}_{AM}^{e,i} = \mathbf{F}_{AM}(s_i, t)$ which is due to the change in motion of the oscillatory flow. Their specific forms are provided in Table 1. Equivalent fluid forces are principally based on the Morison formula (Denny et al., 1998), a semi-empirical formula utilised to determine the forces on slender structures subjected to wave action. $\mathbf{F}^{e,i}$ is extensively employed in the dynamic modelling of underwater flexible beams, but frequently undergoes further simplification. For instance, the component of the additional inertial force in the beam axis direction is neglected due to the utilisation of a non-extensible beam model (Luhar et al., 2016).

As the flexible beam undergoes a significant degree of deformation, the equivalent fluid force acting on the flexible beam is calculated in terms of the relative velocity of the fluid with respect to the flexible beam. This results in the coupling of the motion of the flexible beam with the flow velocity.

Consider the flow field velocity vector at the point P underwater to be $\widehat{\mathbf{U}}(s,t)$. The simplest assumption for describing the flow field velocity can be expressed as,

$$\widehat{\mathbf{U}}_1(s,t) = \begin{pmatrix} 0 \\ U_f\cos(\omega t)\end{pmatrix} \tag{11}$$

where, U_f denotes the maximum oscillatory flow field velocity and ω denotes the oscillatory flow field velocity frequency. Considering the presence of waves, the linear wave theory (Dean and Dalrymple, 1991) can be employed,

$$\widehat{\mathbf{U}}_2(s,t) = \begin{pmatrix} a_w\omega\dfrac{\sinh\left(k_f(s+u_x)\right)}{\sinh(kH)}\sin\left(k_f u_y - \omega t\right) \\ a_w\omega\dfrac{\cosh\left(k_f(s+u_x)\right)}{\sinh(kH)}\cos\left(k_f u_y - \omega t\right)\end{pmatrix} \tag{12}$$

where, a_w denotes the wave amplitude; k_f denotes the wave number, which satisfies the dispersion relation $\omega = \sqrt{gk_f\tanh\left(k_f H\right)}$; $g = 9.81\ \mathrm{m/s^2}$ denotes the gravitational acceleration. In applying linear wave theory to determine the velocity of the flow field, U_f can be set as $a_w\omega\cosh(kl)/\sinh(kH)$, which denotes the maximum velocity of the flow field at the end position when the flexible beam is not deformed.

The following derivation applies to all flow field velocity assumptions and thus $\widehat{\mathbf{U}}$ is still used to denote the flow field velocity vector. Define $\widehat{\mathbf{U}}_{rel}(s,t) = \widehat{\mathbf{U}} - \partial\mathbf{u}/\partial t$ as the relative velocity vector between the flexible beam and the fluid at the point P. Thus, the axial unit vector $\mathbf{T}_t(s,t) = \begin{pmatrix}\cos\varphi & \sin\varphi\end{pmatrix}^T$ and the normal unit vector $\mathbf{T}_n(s,t) = \begin{pmatrix}-\sin\varphi & \cos\varphi\end{pmatrix}^T$ of the flexible beam can be decomposed into the axial relative velocity $U_t(s,t) = \widehat{\mathbf{U}}_{rel}{}^T\cdot\mathbf{T}_t$ and the normal relative velocity $U_n(s,t) = \widehat{\mathbf{U}}_{rel}{}^T\cdot\mathbf{T}_n$.

The equivalent fluid forces require the drag coefficient C_D, inertial coefficient C_M, and friction coefficient C_F. The drag coefficient C_D and the inertial coefficient C_M for the flexible beam depend on the KC, defined as $KC = U_f T_f/b$ where U_f denotes the maximum oscillatory flow field velocity and $T_f = 2\pi/\omega$ denotes the flow field velocity period. Rational functions were used to fit the $C_D(KC)$ and $C_M(KC)$ measured in the experiments (Keulegan and Carpenter, 1958) and used in the calculations,

Table 2
fitting coefficients of $C_D(KC)$ and $C_M(KC)$.

i	p_i^D	q_i^D	p_i^M	q_i^M
0	2.3×10^4	1638	6.795×10^6	5.924×10^6
1	-1129	45.84	-9.433×10^5	-1.602×10^6
2	348.1	66.32	3.313×10^4	1.839×10^5
3	-	-	4267	-8941
4	-	-	-431.6	133.5
5	-	-	10.73	-

$$\begin{cases} C_D = \max\left(\dfrac{\sum_{i=0}^{2} p_i^D (KC)^i}{(KC)^3 + \sum_{i=0}^{2} q_i^D (KC)^i}, 1.95 \right) \\ C_M = \dfrac{\sum_{i=0}^{5} p_i^M (KC)^i}{(KC)^5 + \sum_{i=0}^{4} q_i^M (KC)^i} \end{cases} \tag{13}$$

The specific fitting coefficients are listed in Table 2. The coefficient of determination R^2 (Glantz, 2016) for $C_D(KC)$ and $C_M(KC)$ are 0.9922 and 0.9587, respectively. It should be noted that a direct fit to the experimental data would result in C_D being <1.95 (C_D in steady flow) when KC is relatively large (Luhar and Nepf, 2016). Therefore, in practical calculations, the maximum value of C_D is taken to be 1.95.

The friction coefficient C_F for the flexible beam depends on the Reynolds number (Re), defined as $Re = U_f b / \upsilon_f$, where $\upsilon_f = 1 \times 10^{-6}$ denotes the kinematic viscosity of the water. The friction coefficient $C_F(Re)$ used in the calculation is given by (Zeller et al., 2014),

$$C_F = 0.074 Re^{-0.2} \tag{14}$$

As Fig. 2, the variation of C_D with KC is monotonic and increases rapidly with increasing KC, whereas the variation of C_M with KC is relatively complex, with a non-monotonic interval for C_M at $KC < 20$.

2.2. IHB method

Regardless of the assumptions made about the flow field velocity, the velocity is always periodic, resulting in an eventual periodic motion of the flexible beam in the flow field. The periodic response of the underwater flexible beam can be obtained using the IHB method. The method requires the solution to be expanded into a truncated Fourier series. Then, Eq. (5) is transformed into a nonlinear algebraic equation by harmonic balancing and solved by Newton's method.

Define $\tau = \omega t$ as the non-dimensional time. Upon replacing t by τ, the original differential relationship transforms,

$$\begin{cases} \dfrac{\partial \mathbf{d}^{(n)}}{\partial t} = \omega \dot{\mathbf{d}}^{(n)} \\ \dfrac{\partial^2 \mathbf{d}^{(n)}}{\partial t^2} = \omega^2 \ddot{\mathbf{d}}^{(n)} \end{cases} \tag{15}$$

where, $\dot{\bullet}$ and $\ddot{\bullet}$ denote $\partial \bullet / \partial \tau$ and $\partial^2 \bullet / \partial \tau^2$, respectively. Upon substituting Eq. (15) into Eq. (5), and expanding Eq. (5) around a non-trivial solution $\mathbf{d}_0^{(n)}(\tau)$ using the Taylor expansion, while neglecting high-order terms, it can be obtained,

$$\left(\omega^2 \mathbf{M} - \frac{\partial \mathbf{Q}}{\partial \ddot{\mathbf{d}}^{(n)}}\right)\Big|_{\mathbf{d}_0^{(n)}} \cdot \Delta \ddot{\mathbf{d}}^{(n)} - \frac{\partial \mathbf{Q}}{\partial \dot{\mathbf{d}}^{(n)}}\Big|_{\mathbf{d}_0^{(n)}} \cdot \Delta \dot{\mathbf{d}}^{(n)} + \left(\sum_{\alpha=1}^{3(N^e+1)} \frac{\partial \mathbf{M}}{\partial (\mathbf{d}^{(n)})_\alpha} (\mathbf{d}^{(n)})_\alpha - \frac{\partial \mathbf{Q}}{\partial \mathbf{d}^{(n)}} \right)\Big|_{\mathbf{d}_0^{(n)}} \cdot \Delta \mathbf{d}^{(n)} = -\mathbf{r} \tag{16}$$

where, $()_\alpha$ denotes the αth entry of a vector; $\Delta \mathbf{d}^{(n)} = \mathbf{d}^{(n)} - \mathbf{d}_0^{(n)}$;$\mathbf{r}\left(\mathbf{d}^{(n)}, \dot{\mathbf{d}}^{(n)}, \ddot{\mathbf{d}}^{(n)}, \tau\right) = \omega^2 \mathbf{M} \cdot \ddot{\mathbf{d}}^{(n)} - \mathbf{Q}\left(\mathbf{d}^{(n)}, \dot{\mathbf{d}}^{(n)}, \ddot{\mathbf{d}}^{(n)}, \tau\right)$ denotes residual vector. The specific forms of $\partial \mathbf{Q}/\partial \mathbf{d}^{(n)}$, $\partial \mathbf{Q}/\partial \dot{\mathbf{d}}^{(n)}$, $\partial \mathbf{Q}/\partial \ddot{\mathbf{d}}^{(n)}$ and $\partial \mathbf{M}/\partial (\mathbf{d}^{(n)})_\alpha$ are in Appendix A. The entry of $\mathbf{d}^{(n)}$ and $\Delta \mathbf{d}^{(n)}$ can be expressed using Fourier series, respectively,

$$\begin{aligned} (\mathbf{d}^{(n)})_\alpha &= a_\alpha^0 + \sum_{i=1}^{N^f} a_\alpha^i \cos(i\tau) + b_\alpha^i \sin(i\tau) \\ &= \mathbf{C} \cdot \mathbf{P}_\alpha \end{aligned} \tag{17}$$

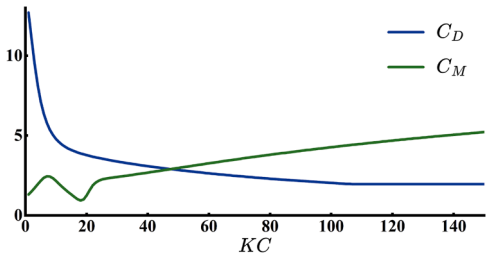

Fig. 2. Fitted curves of $C_D(KC)$ and $C_M(KC)$ with KC.

$$\begin{aligned}(\Delta\mathbf{d}^{(n)})_\alpha &= \Delta a_\alpha^0 + \sum_{i=1}^{N^f} \Delta a_\alpha^i \cos(i\tau) + \Delta b_\alpha^i \sin(i\tau) \\ &= \mathbf{C}\cdot\Delta\mathbf{P}_\alpha\end{aligned} \tag{18}$$

where, N^f denotes the truncation number; $\mathbf{C}(\tau) = \begin{pmatrix}1 & \cos\tau & \sin\tau & \cdots & \cos i\tau & \cos i\tau & \cdots & \cos N^f\tau & \cos N^f\tau\end{pmatrix}$ denotes the trigonometric base row vector; $\mathbf{P}_\alpha = \begin{pmatrix}a_\alpha^0 & a_\alpha^1 & b_\alpha^1 & \cdots & a_\alpha^i & b_\alpha^i & \cdots & a_\alpha^{N^f} & b_\alpha^{N^f}\end{pmatrix}^T$ and $\Delta\mathbf{P}_\alpha = \begin{pmatrix}\Delta a_\alpha^0 & \Delta a_\alpha^1 & \Delta b_\alpha^1 & \cdots & \Delta a_\alpha^i & \Delta b_\alpha^i \cdots \Delta a_\alpha^{N^f} \Delta b_\alpha^{N^f}\end{pmatrix}^T$ denote the corresponding coefficient vector. Thus, it can be obtained that $\mathbf{d}^{(n)}(\tau) = \mathbf{C}^g\cdot\mathbf{P}$ and $\Delta\mathbf{d}^{(n)}(\tau) = \mathbf{C}^g\cdot\Delta\mathbf{P}$, where $\mathbf{C}^g(\tau) = \mathrm{diag}(\overbrace{\mathbf{C},\ldots,\mathbf{C}}^{3(N^e+1)})$, $\mathbf{P} = \begin{pmatrix}\mathbf{P}_1{}^T & \cdots & \mathbf{P}_{3(N^e+1)}{}^T\end{pmatrix}^T$ and $\Delta\mathbf{P} = \begin{pmatrix}\Delta\mathbf{P}_1{}^T & \cdots & \Delta\mathbf{P}_{3(N^e+1)}{}^T\end{pmatrix}^T$. Similarly, the first-order and second-order derivatives of $\mathbf{d}^{(n)}$ are $\dot{\mathbf{d}}^{(n)}(\tau) = \dot{\mathbf{C}}^g\cdot\mathbf{P}$ and $\ddot{\mathbf{d}}^{(n)}(\tau) = \ddot{\mathbf{C}}^g\cdot\mathbf{P}$, respectively; The first-order and second-order derivatives of $\Delta\mathbf{d}^{(n)}$ are $\Delta\dot{\mathbf{d}}^{(n)}(\tau) = \dot{\mathbf{C}}^g\cdot\Delta\mathbf{P}$ and $\Delta\ddot{\mathbf{d}}^{(n)}(\tau) = \ddot{\mathbf{C}}^g\cdot\Delta\mathbf{P}$, respectively. Thus, the ε^n and φ^n on the nth node can be obtained,

$$\begin{cases}\varepsilon^n = a_n^{0,\varepsilon} + \sum_{i=1}^{N^f} a_n^{i,\varepsilon}\cos(i\tau) + b_n^{i,\varepsilon}\sin(i\tau) \\ \qquad\quad = \mathbf{C}\cdot\mathbf{P}_n^\varepsilon \\ \varphi^n = a_n^{0,\varphi} + \sum_{i=1}^{N^f} a_n^{i,\varphi}\cos(i\tau) + b_n^{i,\varphi}\sin(i\tau) \\ \qquad\quad = \mathbf{C}\cdot\mathbf{P}_n^\varphi\end{cases} \tag{19}$$

The harmonic balance procedure is then conducted. Substituting Eq. (17) and Eq. (18) into Eq. (16), Pre-multiplying Eq. (16) by $\mathbf{C}^{gT}$, and integrating the resulting equations from 0 to 2π yield,

$$\mathbf{J}\cdot\Delta\mathbf{P} = \mathbf{R} \tag{20}$$

where,

$$\mathbf{J} = \frac{1}{\pi}\int_0^{2\pi} \mathbf{C}^{gT}\cdot\left(\left(\omega^2\mathbf{M} - \frac{\partial\mathbf{Q}}{\partial\ddot{\mathbf{d}}^{(n)}}\right)\Big|_{\mathbf{d}_0^{(n)}}\cdot\ddot{\mathbf{C}}^g - \frac{\partial\mathbf{Q}}{\partial\dot{\mathbf{d}}^{(n)}}\Big|_{\mathbf{d}_0^{(n)}}\cdot\dot{\mathbf{C}}^g + \left(\sum_{\alpha=1}^{3(N^e+1)}\frac{\partial\mathbf{M}}{\partial(\mathbf{d}^{(n)})_\alpha}(\mathbf{d}^{(n)})_\alpha - \frac{\partial\mathbf{Q}}{\partial\mathbf{d}^{(n)}}\right)\Big|_{\mathbf{d}_0^{(n)}}\cdot\mathbf{C}^g\right)\mathrm{d}\tau \tag{21}$$

denotes the Jacobi matrix and

$$\mathbf{R} = -\frac{1}{\pi}\int_0^{2\pi}\left(\mathbf{C}^{gT}\cdot\mathbf{r}\right)\mathrm{d}\tau \tag{22}$$

denotes the residual vector.

If an initial guess of $\mathbf{d}^{(n)}$ is made, Newton iterations can continue until the norm of $\mathbf{R}$ is less than a preset tolerance, thereby obtaining a periodic solution of Eq. (5). To circumvent the necessity of directly calculating Galerkin integrals when generating $\mathbf{J}$ and $\mathbf{R}$, the EGA procedure is employed. A comprehensive account of the EGA procedure can be found in Ju et al. (2020), which offers a more expedient approach than that of Eq. (21), Eq. (22), for the computation of $\mathbf{J}$ and $\mathbf{R}$.

2.3. Arc-length continuation method

A response curve is a commonly employed tool for elucidating the variation in periodic response amplitudes as a function of a specific parameter, such as the external excitation frequency or a structural parameter. The continuation method (Ri et al., 2020) has been a prevalent approach for obtaining response curves in nonlinear dynamic analysis, as it can circumvent the occurrence of singular points at their peaks.

Define S as the arc-length parameter and $\mathbf{X} = \begin{pmatrix}\mathbf{P}^T & \omega\end{pmatrix}^T$. Given that the number of unknowns in $\mathbf{X}$ exceeds that of the equations in Eq. (5), the following augmented equation is employed (Woiwode et al., 2020),

$$g(\mathbf{X}) - S = 0 \tag{23}$$

where, $g(\mathbf{X}) = (\mathbf{X}_p - \mathbf{X}_b)^T\cdot(\mathbf{X} - \mathbf{X}_p) / \|\mathbf{X}_p - \mathbf{X}_b\|$, which $\mathbf{X}_p$ denotes the previous solution vector on the response curve and $\mathbf{X}_b$ denotes the solution vector before the previous one. In terms of Newton iterations, the following relationship holds,

$$\begin{pmatrix}\mathbf{J} & \mathbf{R}^\omega \\ \mathrm{d}g/\mathrm{d}\mathbf{X}^T\end{pmatrix}\cdot\begin{pmatrix}\Delta\mathbf{X} \\ \Delta\omega\end{pmatrix} = \begin{pmatrix}\mathbf{R} \\ g(\mathbf{X}) - S\end{pmatrix} \tag{24}$$

where, $\mathbf{R}^\omega = -\frac{1}{\pi}\int_0^{2\pi}\left(\mathbf{C}^{gT}\cdot\frac{\partial\mathbf{r}}{\partial\omega}\right)\mathrm{d}\tau$. After solving Eq. (24), $\mathbf{X}$ is updated by $\mathbf{X} + \Delta\mathbf{X}\rightarrow\mathbf{X}$ and ω is updated by $\omega + \Delta\omega\rightarrow\omega$.

2.4. Stability analysis

Once a steady-state periodic response of the underwater flexible beam has been obtained using the EGA-IHB method, an analysis of its stability is required. This is typically conducted using Floquet theory (Cheung et al., 1990), which involves introducing a minor perturbation to the steady-state periodic solution. Assume $\mathbf{d}_*^{(n)}(\tau)$ is the steady-state solution that satisfies Eq.(5) and $\delta\mathbf{d}^{(n)}(\tau)$ is a small perturbation around $\mathbf{d}_*^{(n)}$. Using the Taylor expansion while neglecting high-order terms, the following result is obtained,

$$\left(\omega^2\mathbf{M}-\frac{\partial\mathbf{Q}}{\partial\ddot{\mathbf{d}}^{(n)}}\right)\Big|_{\mathbf{d}_*^{(n)}}\cdot\delta\ddot{\mathbf{d}}^{(n)}-\frac{\partial\mathbf{Q}}{\partial\dot{\mathbf{d}}^{(n)}}\Big|_{\mathbf{d}_*^{(n)}}\cdot\delta\dot{\mathbf{d}}^{(n)}+\left(\sum_{\alpha=1}^{3(N^e+1)}\frac{\partial\mathbf{M}}{\partial(\mathbf{d}^{(n)})_\alpha}(\mathbf{d}^{(n)})_\alpha-\frac{\partial\mathbf{Q}}{\partial\mathbf{d}^{(n)}}\right)\Big|_{\mathbf{d}_*^{(n)}}\cdot\delta\mathbf{d}^{(n)}=0 \tag{25}$$

Transforming Eq. (25) to a state-space form with a state-space variable $\mathbf{Y}(\tau)=\left(\mathbf{Y}_1{}^T\quad\mathbf{Y}_2{}^T\right)^T$, where $\mathbf{Y}_1=\delta\mathbf{d}^{(n)}$ and $\mathbf{Y}_2=\mathrm{d}\delta\mathbf{d}^{(n)}/\mathrm{d}\tau$. The stability of Eq.(24) can be evaluated by calculating the eigenvalues of the transformation matrix $\mathbf{B}$ that transforms $\mathbf{Y}$ at $\tau=0$ to that at $\tau=2\pi$. The transformation matrix $\mathbf{B}$ can be computed using Hsu's method in $\mathbf{B}=\sum_{k=1}^{N^T}\exp\left(\mathbf{\Phi}\left(\frac{2\pi}{N^T}k\right)\frac{2\pi}{N^T}\right)$, where N^T denotes the number of equal divisions of the period. The periodic matrix $\mathbf{\Phi}(\tau)$ is given by,

$$\mathbf{\Phi}=\begin{pmatrix}\mathbf{0} & \mathbf{I}\\ \widehat{\mathbf{M}}^{-1}\cdot\widehat{\mathbf{K}}^0 & \widehat{\mathbf{M}}^{-1}\cdot\widehat{\mathbf{K}}^1\end{pmatrix} \tag{26}$$

where, $\widehat{\mathbf{M}}(\tau)=\left(\omega^2\mathbf{M}-\frac{\partial\mathbf{Q}}{\partial\ddot{\mathbf{d}}^{(n)}}\right)\Big|_{\mathbf{d}_*^{(n)}}$; $\widehat{\mathbf{K}}^0(\tau)=\left(\sum_{\alpha=1}^{3(N^e+1)}\frac{\partial\mathbf{M}}{\partial(\mathbf{d}^{(n)})_\alpha}(\mathbf{d}^{(n)})_\alpha-\frac{\partial\mathbf{Q}}{\partial\mathbf{d}^{(n)}}\right)\Big|_{\mathbf{d}_*^{(n)}}$; $\widehat{\mathbf{K}}^1(\tau)=-\frac{\partial\mathbf{Q}}{\partial\dot{\mathbf{d}}^{(n)}}\Big|_{\mathbf{d}_*^{(n)}}$. If all the eigenvalues of $\mathbf{B}$ are inside the unit circle in the complex plane, the periodic solution is stable; otherwise, it is unstable.

3. Experiments and validations of numerical model

The experiments were conducted in a recirculation water channel at the University of Texas at Dallas. The water tunnel has a test section of 2 m length and 200 mm width with a background turbulence level of <1 % (Suresh et al., 2021; Aju et al., 2022). A 0.5 mm thickness acrylic flexible beam (Young's modulus $E=3.2$ GPa) with length $l=15$ cm and width $d=20$ mm was mounted in the middle of the water channel bed as shown in Fig. 3**(a)**. The flexible beam was submerged inside the water and maintained a 50 mm gap between its free end and the water surface without bending. The design of the wave generator is also illustrated in Fig. 3**(a)**.

The variations in streamwise velocity were achieved by moving an 80 μm stainless mesh mounted on a high torque motor-driven transverse system. Forward movements of the mesh decelerated the incoming flow, while backward movements accelerated it. To ensure a more uniform flow, this traverse system was positioned 40 cm downstream of the flexible beam, the target was to generate a sinusoidal wave form depicted as $u(t)=U_0(1+\delta\sin(\omega t))$, where U_0 denotes the mean incoming flow field velocity generated by the water channel and δ denotes flow field velocity amplitude ratio. The motion of the frame was programmed to follow a trajectory defined by $x_\omega(t)=\sigma_\omega\sin(2\pi f_\omega t)$ in order to generate the sinusoidal waves with different wave amplitudes and frequencies, where f_ω is frequency of the moving net and σ_ω is the moving frame amplitude. The transfer function $U_1=\delta U_0=f(U_0,\sigma_\omega)$ was calibrated by measuring the averaged velocity near the location of the flexible beam centre, and each calibration data point then was used as the training points for Radial Basis Function Method to generate the function surface $U_1=f(U_0,\sigma_\omega)$. With this calibrated function, we were able to realize the desire U_1 and ω by adjusting parameters in the traverse system. To capture the flow field and verify the flow uniformity, a planar particle image velocimetry (PIV) system from TSI was applied to characterize the wave velocity. A field of view (FOV) of 135 mm × 84 mm was illuminated via a 1 mm thick laser sheet from a 30 mJ/pulse laser. The water flow was seeded with 14 μm silver-coated hollow glass spheres with a density of 1.02 g /cm^{-3}. The image pairs were captured with a 4 MP (2560 ×1600 mm pixels), 16-bit CMOS camera at a frequency of 60 Hz. Fig. 3**(b)** shows a sample case of the velocity along the depth-wise direction. The reciprocating motion of the wave generator was set to 0.1 Hz, and the target flow is $u(t)=0.136(1+0.23\sin(0.2\pi t))$ m /s. The

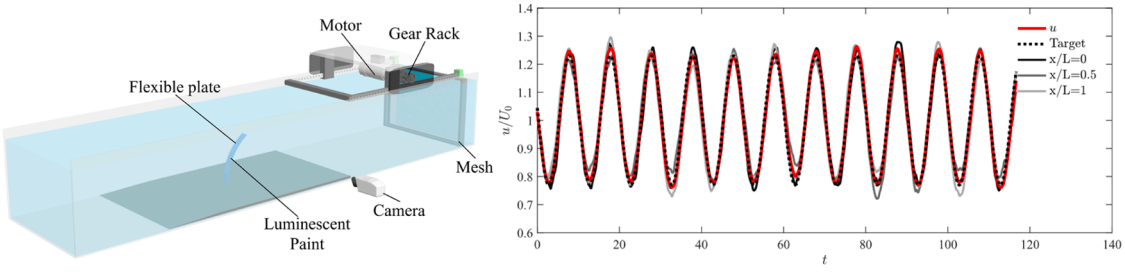

Fig. 3. (a) Schematic of the experiment set up. (b) Verification of the generated flow uniformity. The red solid line is the space averaged time series for the incoming velocity along the wall-normal direction, dark dash line represents the target flow velocity function $u(t)=0.136(1+0.23\sin(0.2\pi t))$ m /s, the grey solid lines show the time series at 3 different depths.

experimental results demonstrated a good fitting with the target flow time series along the height of the flexible beam. The motion of the flexible beam was captured by a high-speed camera from DANTEC at a sampling frequency of 60 Hz. To facilitate the detection of beam vibrations, the side of the flexible beam facing the camera was painted by a luminous paint. A total of 8 sets of experiments were performed under different oscillating flow scenarios as shown in Fig. 4 and Fig. 5. In the numerical calculations, the flow field velocity assumption $\widehat{\mathbf{U}}^{*} = (0 \quad U_0(1+\delta\sin(\omega t)))^T$ is used and the C_D is set to 1.95 due to the effect of the current component. The numerical results demonstrate reasonable agreement with the experimental results. In order to quantitatively assess the error situation between simulation and experiment, the horizontal and vertical relative errors are defined as $e_h = (e_{s,h} - e_{e,h})/e_{e,h}$ and $e_v = (e_{s,v} - e_{e,v})/e_{e,v}$, where $e_{s,h}$, $e_{e,h}$ denote the maximum horizontal displacement of simulation and experiment, respectively, and $e_{s,v}$, $e_{e,v}$ denote the maximum vertical displacement of simulation and experiment, respectively. It is worth noting that for the beam tested in the experiments, its first-order natural frequency was 6.6 Hz, which was more than one order of magnitude higher than the highest f_ω examined in the water channel. Therefore, the beam oscillations were dominated by the first-order deformations.

4. Numerical results

This work aims to examine the amplitude-frequency characteristics of flexible beams under different oscillatory flows. In the parametric study, $T_f = 0.5 - 20$ s which corresponds $\omega = 0.1\pi - 4\pi$ rad/s. In the case based on $\widehat{\mathbf{U}}_1$, $U_f = 1 - 15$ cm/s. Thus, $KC = 0.25 - 150$; $Re = 200 - 3000$. In the case based on $\widehat{\mathbf{U}}_2$, $a_w = 5 - 35$ mm/s. Thus, $U_f = 0.252 - 17.32$ cm/s; $KC = 0.063 - 173.2$; $Re = 50.32 - 3463$. In the numerical calculations, $N^e = 35$; $N^f = 25$.

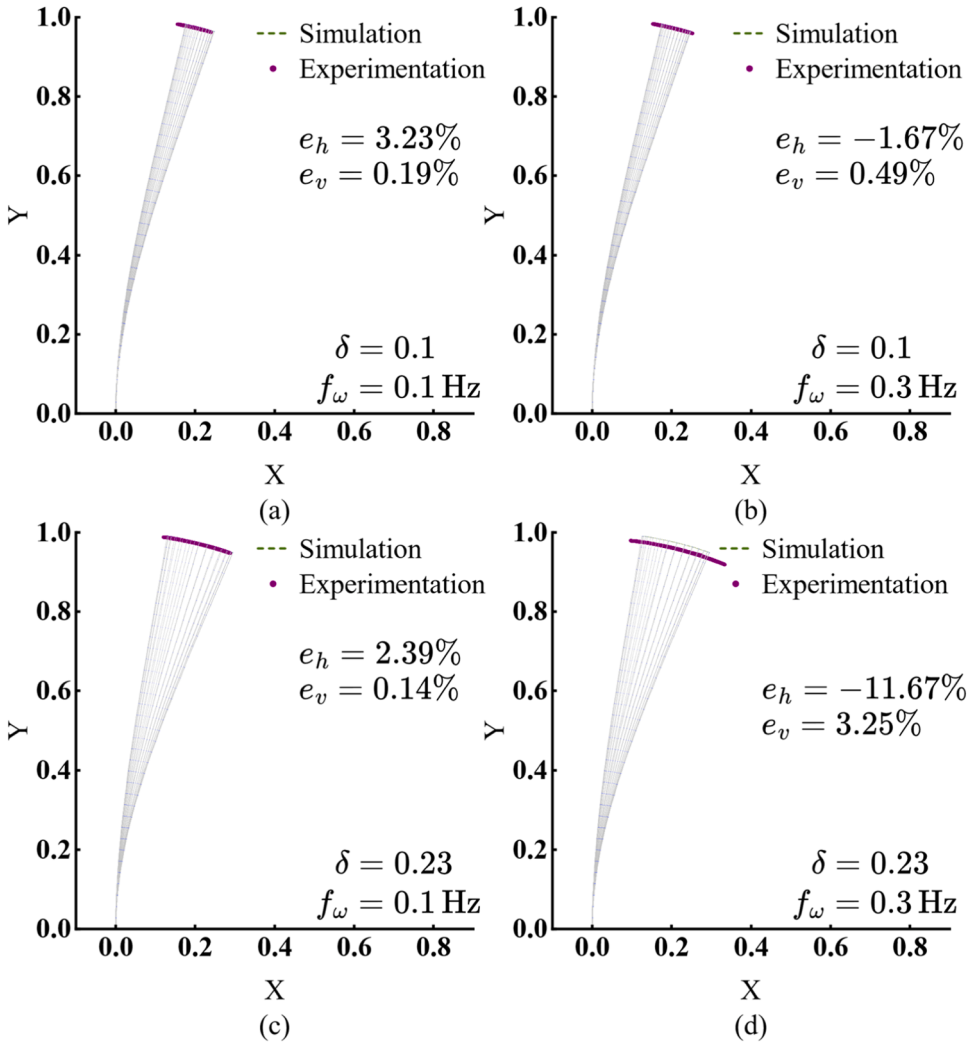

Fig. 4. Comparison of experimental and numerical results. Snapshots of the motion (simulation) and trajectories (experimentation) of the flexible beam for one cycle under $U_0 = 0.136$ m/s.

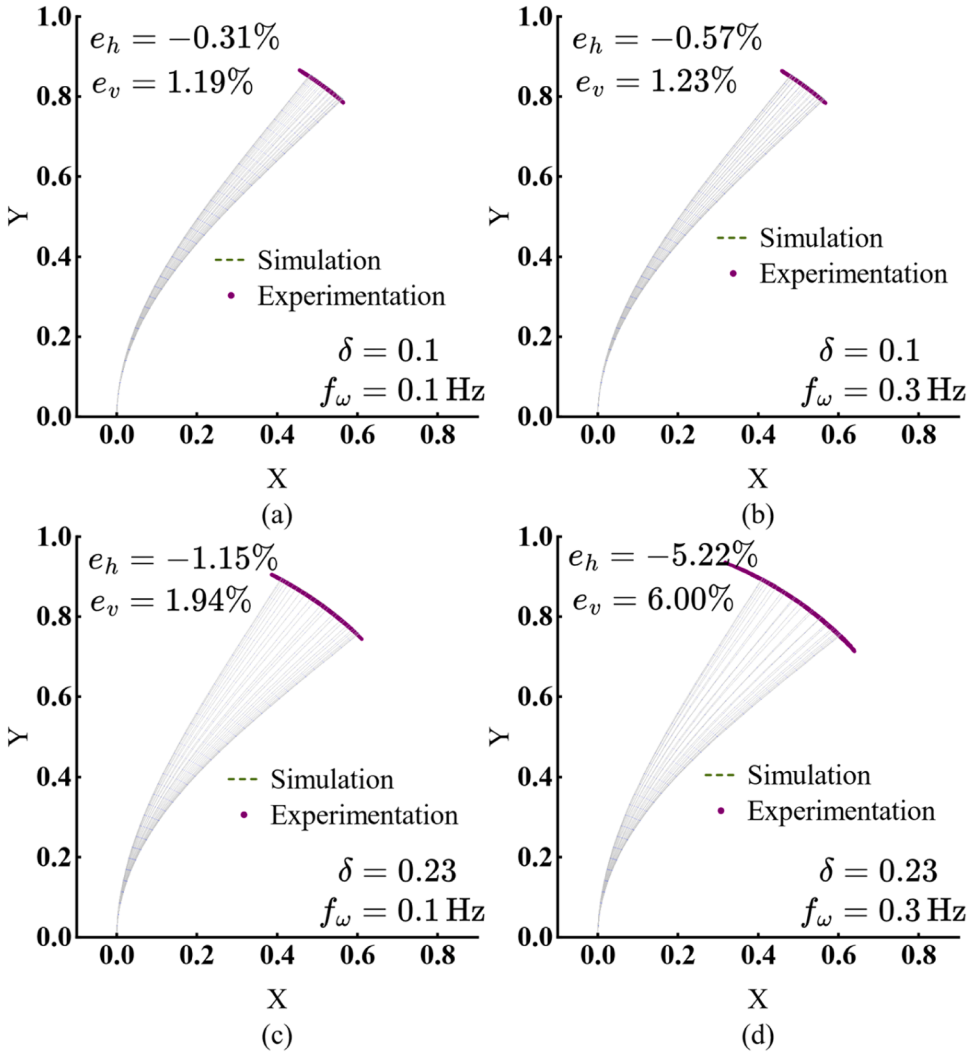

Fig. 5. Comparison of experimental and numerical results. Snapshots of the motion (simulation) and trajectories (experimentation) of the flexible beam for one cycle under $U_0 = 0.284\,\mathrm{m/s}$.

The numerical results of the dynamics model are based on three specifications of flexible beam: high-density polyethene (HDPE, $E = 0.93\,\mathrm{GPa}$, $\rho = 950\,\mathrm{kg/m^3}$, and $h = 0.4\,\mathrm{mm}$), low-density polyethene (LDPE, $E = 0.3\,\mathrm{GPa}$, $\rho = 920\,\mathrm{kg/m^3}$, and $h = 0.4\,\mathrm{mm}$). The remaining physical parameters are as follows: $H = 40\,\mathrm{cm}$, $\rho_f = 1000\,\mathrm{kg/m^3}$, $b = 2\,\mathrm{cm}$, $l = 20\,\mathrm{cm}$, and $\alpha = 0.002$. Although the mass density of the HDPE and LDPE materials is approximately equal to that of water, the inertial force on the flexible beams is mainly provided by the flow field due to the added inertial force $\propto \frac{\pi}{4}\rho_f b^2 C_M$, which is typically much more significant than ρbh.

To quantitatively describe the steady-state dynamic response of the flexible beam, defining the amplitude of the frequency response of the tensile strain ε and bending strain κ in the axis of the flexible beam,

$$\Sigma^{\{\varepsilon,\kappa\}} = \sqrt{\sum_{n=1}^{N^e+1}\left(\left(a_n^{0,\{\varepsilon,\kappa\}}\right)^2 + \sum_{i=1}^{N^f}\left(a_n^{i,\{\varepsilon,\kappa\}}\right)^2 + \left(b_n^{i,\{\varepsilon,\kappa\}}\right)^2\right)} \tag{27}$$

Also, defining the force-frequency response of the added inertial force and the drag force,

$$\Sigma^{\{m,d\}} = \sqrt{\sum_{n=1}^{N^e+1}\left(\left(a_n^{0,\{m,d\}}\right)^2 + \sum_{i=1}^{N^f}\left(a_n^{i,\{m,d\}}\right)^2 + \left(b_n^{i,\{m,d\}}\right)^2\right)} \tag{28}$$

where, $a_n^{i,\{m,d\}}$ and $b_n^{i,\{m,d\}}$ are harmonic coefficients of $\mathbf{Q}_m^{e,i} = \mathbf{M}_x^{e,i^T} \cdot \left(F_{x,AM}^{e,i} + F_{x,VB}^{e,i}\right) + \mathbf{M}_y^{e,i^T} \cdot \left(F_{y,AM}^{e,i} + F_{y,VB}^{e,i}\right)$ and $\mathbf{Q}_d^{e,i} = \mathbf{M}_x^{e,i^T} \cdot F_{x,D}^{e,i} +$

$\mathbf{M}_y^{e,i^T} \cdot F_{y,D}^{e,i}$, respectively, which $\left\{ F_{x,\{AM,VB,D\}}^{e,i} \quad F_{y,\{AM,VB,D\}}^{e,i} \right\}^T = \mathbf{F}_{\{AM,VB,D\}}(s_i, t)$.

As shown in Fig. 6, the amplitude-frequency characteristic curves of flexible beams under different flow field conditions exhibit multiple resonance phenomena. With the increase in U_f, the low-order resonances (for HDPE, $\omega \approx 0.40 - 1.07$ Hz; for LDPE, $\omega \approx 0.34 - 1.17$ Hz) exhibit the hardening effect, predominantly attributable to the geometric nonlinearity. As the deformation of the flexible beam increases, the internal stress leads to a consequent rise in its structural stiffness, which results in higher resonance frequencies. In different, the amplitude-frequency characteristic curves for higher-order resonances (for HDPE, $\omega \approx 5.20 - 8.83$ Hz, $\omega \approx 7.54 - 10.63$ Hz; for LDPE, $\omega \approx 3.27 - 4.84$ Hz, $\omega \approx 6.62 - 12.02$ Hz, and $\omega \approx 4.21 - 6.13$ Hz) exhibit the softening effect followed by the hardening effect with the increase in U_f. This phenomenon can be understood because of the combined influence of inertia and geometric nonlinearity. At lower U_f, the inertia is predominant, leading to a reduction in resonance frequencies which means the softening effect. As U_f increases further, the geometric nonlinearity is gradually enhanced, ultimately resulting in the hardening effect.

Snapshots of motion in Fig. 7 further show that apart from Fig. 7.**a.1** and Fig. 7.**b.4**, which distinctly showcase the typical motion patterns of the first and second vibration modes of the flexible beam, most of the periodic motions exhibit the mixture of both first and

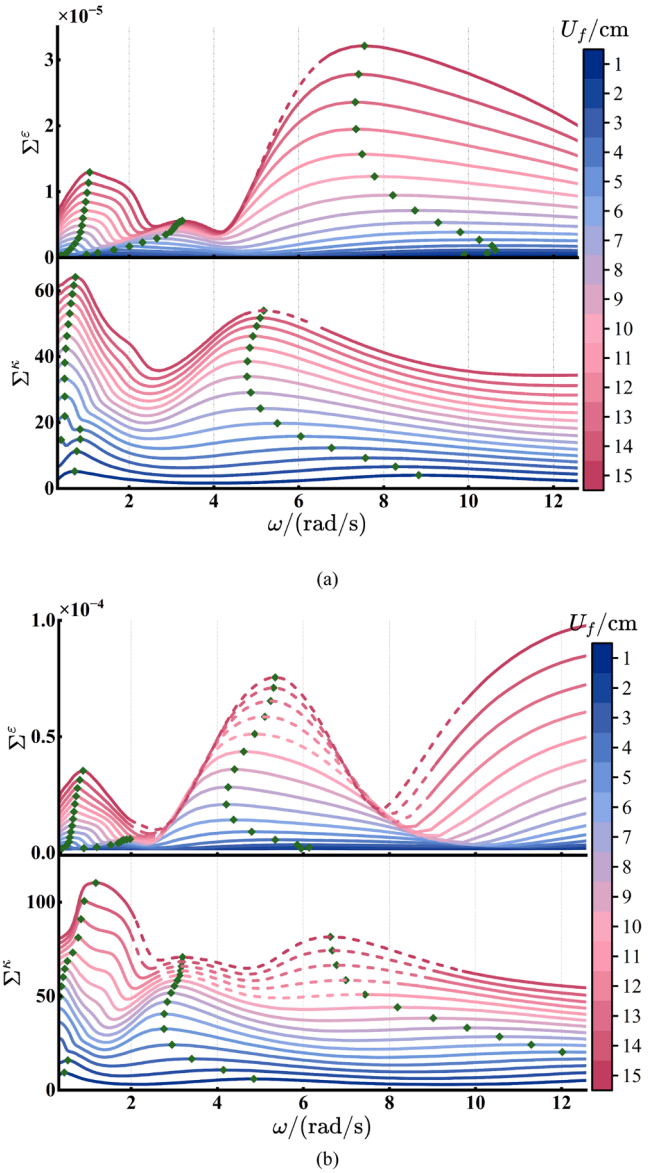

Fig. 6. The amplitude-frequency characteristic curves of flexible beams under different flow field conditions based on $\widetilde{\mathbf{U}}_1$ are presented in subplots (a) and (b), which correspond to HDPE and LDPE materials, respectively. The two coordinate regions of each subplot demonstrate the relationship between ε and κ as a function of ω, with solid lines indicating stable motion and dashed lines indicating unstable motion. Peaks on the amplitude-frequency curves are marked by green diamond-shaped blocks.

second mode characteristics. This suggests that the vibration behaviour of the flexible beam is generally the result of multi-modal coupling rather than being dominated by a single vibration mode.

In the low-frequency range, the resonance of tensile and bending deformations occurs concurrently, indicating a strong coupling between these two deformations at low frequencies. However, as the flow frequency increases, the resonance frequencies of the tensile and bending deformations become increasingly distinct. This separation is likely related to the difference between the tensile and bending stiffnesses and influenced by the interaction of fluid forces and the flexible beam.

In conjunction with the force amplitude-frequency response curves illustrated in Fig. 8, the tensile deformation of the flexible beam is almost entirely dominated by the inertial force. The reason is that the axial component of the inertial force is significantly greater than the axial friction in the fluid resistance. In different, the bending deformation is influenced by both the inertia and the fluid resistance. The peak of the fluid resistance is insufficient to initiate the bending deformation resonance, and a certain level of inertial force is still necessary to excite the bending resonance.

The stability analysis shows that there are unstable regions in amplitude-frequency characteristic curves of the flexible beam. The frequency range of the unstable region expands as U_f increases. This phenomenon may be related to the relationship between inertia and structural stiffness, as HDPE and LDPE have almost the same density, but Young's modulus of LDPE is only 1/3 of that of HDPE.

There is a significant difference between the amplitude-frequency characteristic curves based on $\widehat{\mathbf{U}}_2$ (Fig. 9) and those based on $\widehat{\mathbf{U}}_1$ (Fig. 6). Geometrical nonlinearities have a more significant influence on the amplitude-frequency characteristics. Although inertia can still dominate the specific a_w for flexible beams made of LDPE with low structural stiffness, the range of this specific a_w becomes smaller.

From the snapshots of motion in Fig. 10, the coupling of the vibrational modes of each order of the flexible beam in its mode of motion is enhanced. In addition, the periodic motion of the flexible beam, driven by the symmetrically varying flow field velocity, is asymmetric. The asymmetry of the periodic motion becomes more significant as the structural stiffness and aw of the flexible beam increase, which is consistent with the conclusion of the existing study (Zhu et al., 2020). Combined with the amplitude-frequency characteristic curves in Fig. 9, it is also found that the asymmetry significantly expands the frequency range of resonance of the flexible beam, ultimately leading to the appearance of bifurcation.

The amplitude-frequency characteristic curves calculated based on $\widehat{\mathbf{U}}_2$, the frequency ranges in which the tensile deformation resonance and the bending deformation resonance of the flexible beam occur overlap to a large extent, indicating that the degree of coupling between the two types of deformation is also greater than in the case which calculated based on $\widehat{\mathbf{U}}_1$. From the force amplitude-frequency characteristic curves in Fig. 11, the tensile deformation of the flexible beam is still almost completely dominated by the additional inertial force of the fluid. However, the cause of the resonance of the bending deformation becomes more complex, especially between $a_w = 19 \sim 21$ cm, where there is a significant jump in the frequency of the flow field velocity that leads to the occurrence of the resonance, which is a result of the interaction between the asymmetry of the motion of the flexible beam, the resonance of the tensile deformation and the resonance of the bending deformation.

At higher ω, the deformation of the flexible beam motion becomes smaller and smaller, and its asymmetry gradually disappears.

The presence of two resonances in a narrow frequency range on the amplitude-frequency characteristic curve of the flexible beam at low ω and U_f may be attributed to the fact that the KC corresponding to ω and U_f at this time is situated within a non-monotonic interval on $C_M(KC)$.

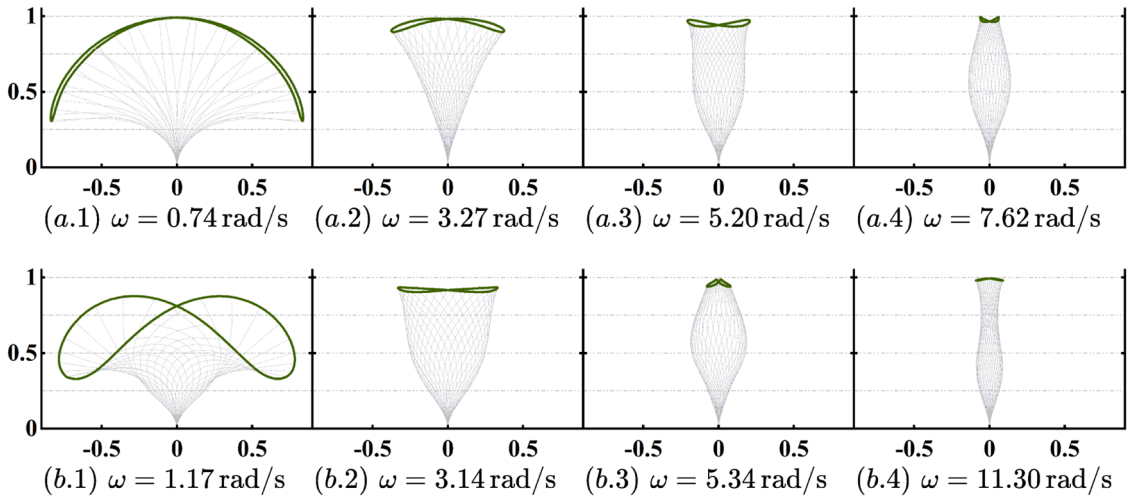

Fig. 7. Snapshots of the motion of the flexible beam for one cycle under different wave period conditions in subplots (a) and (b), which correspond to HDPE and LDPE materials, respectively. The U_f based on $\widehat{\mathbf{U}}_1$ is 15 cm. The coordinate regions represent the OXY plane where the beam is located and the coordinate scale is normalised by the length of the flexible beam. The green curve represents the trajectory of the flexible beam end.

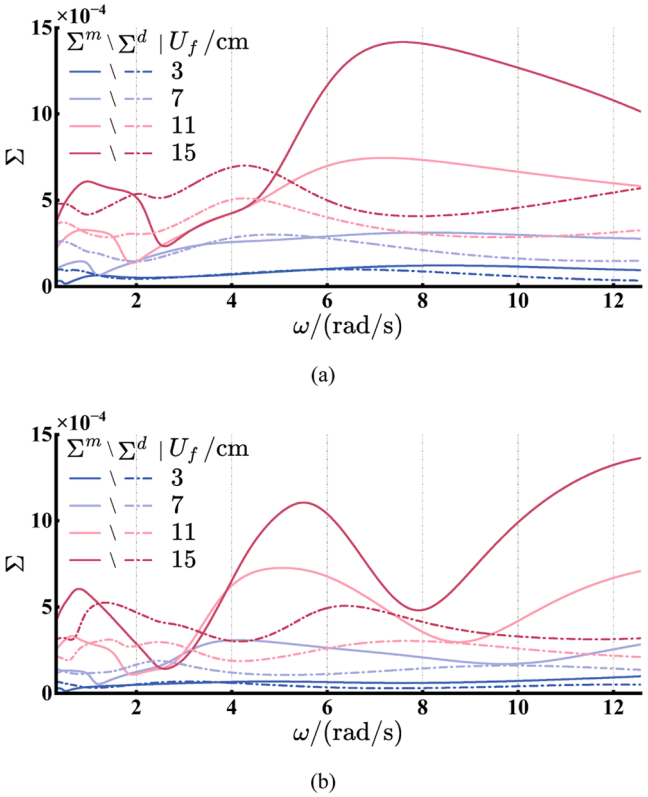

Fig. 8. The force amplitude-frequency characteristic curves of flexible beams under 4 kinds of different flow field conditions based on $\widehat{\mathbf{U}}_1$ are presented in subplots (a) and (b), which correspond to HDPE and LDPE materials, respectively.

Ca (defined as $Ca = \frac{\rho_f b U_f^2 l^3}{EI}$), similar to *KC*, is another dimensionless parameter in this work. Figs. 12–15 illustrate the relationships between responses of the tensile and bending and the parameters *KC* and *Ca*, respectively. Overall, as the value of *Ca* increases, the responses of the flexible beam also intensify. In the case of $\widehat{\mathbf{U}}_1$ (Fig. 12 and Fig. 13), the tensile response and bending response are pronounced when the value of *KC* is low, and over the small range of values of *KC*, there are two peaks with higher levels of both. With a further increase in the value of *KC*, the levels of tensile response and bending response slowly increase first and then decrease. However, the peak of the bending response at a higher value of *KC* increases significantly with increasing values of *Ca* to the point where it exceeds the peak at a lower value of *KC*. In the case of $\widehat{\mathbf{U}}_2$, the tensile and bending responses varied relatively consistently with values of *KC* and *Ca*. At a lower value of *KC*, both responses have higher levels. For the tensile response, the level increases and then decreases as the value of *KC* continues to increase. However, at a higher value of *Ca*, the tensile response exhibits two peaks within the range of high values of *KC*.

5. Conclusion

This work presents an in-depth analysis of the nonlinear steady-state dynamics of a flexible beam subjected to an oscillatory flow, with numerical simulations based on two different flow field velocity assumptions ($\widehat{\mathbf{U}}_1$ and $\widehat{\mathbf{U}}_2$). For a strongly nonlinear system of partial differential equations based on the theory of the large deformation beam allowing tensile deformations and fluid dynamics, the spatial domains and temporal domains discretisation is performed using high-order FEM and IHB, respectively, combined with the arc length extension method and Hsu's method for continuum tracking of solutions and stability discrimination. Actual physical experiments verify the correctness of the method. The effects of significant flow velocity and flow velocity change frequency on the dynamic response of flexible beams are investigated, and various typical nonlinear phenomena, such as the soft and hardening effects, are observed.

In contrast to previous studies, the results of this work show that flexible beams subjected to oscillatory flow also undergo resonance phenomena for their tensile deformation. Although there is no coupling between the tensile and bending deformations of the flexible beams from a modelling point of view (since the beams are composed of mono materials and have a rectangular cross-section), the resonance of the tensile deformations is still triggered under certain conditions due to the complex loading conditions. It is strongly coupled with the resonance of the bending deformations.

The action of the fluid on the flexible beam is complex. Although the analyses in this work consider only the unidirectional action of

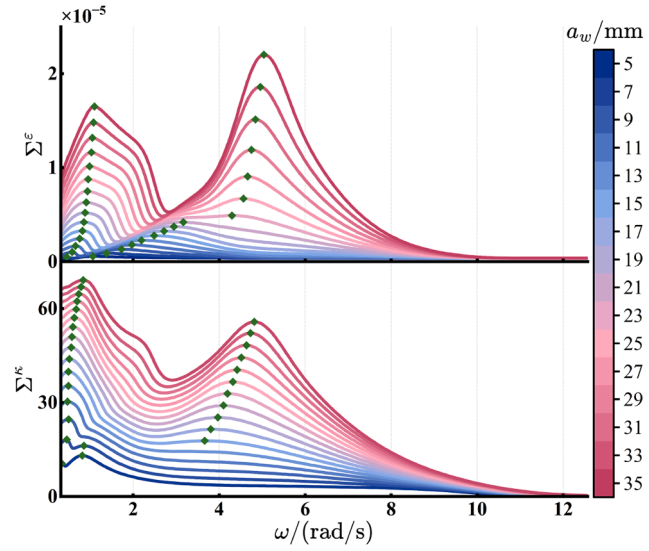

(a)

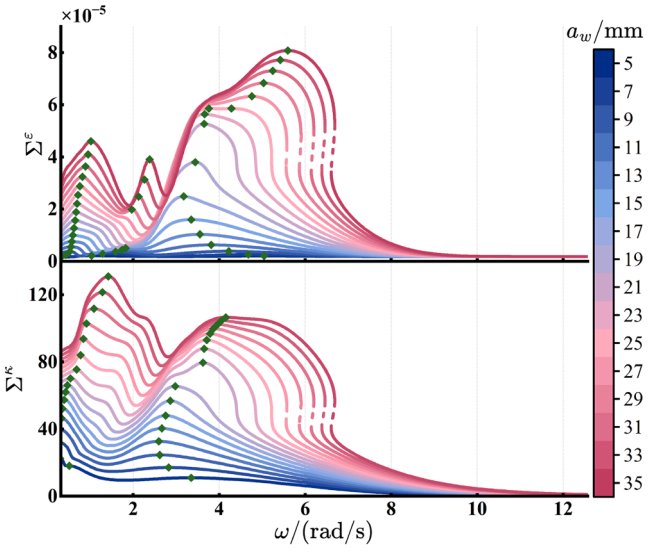

(b)

Fig. 9. The amplitude-frequency characteristic curves of flexible beams under different flow field conditions based on $\widetilde{\mathbf{U}}_2$ are presented in subplots (a) and (b), which correspond to HDPE and LDPE materials, respectively. The two coordinate regions of each subplot demonstrate the relationship between ε and κ as a function of ω, with solid lines indicating stable motion and dashed lines indicating unstable motion. Peaks on the amplitude-frequency curves are marked by green diamond-shaped blocks.

the fluid on the flexible beam and ignore the counteraction of the flexible beam on the fluid, this simplified treatment is still reasonable regarding the degree of agreement of the experimental results. Moreover, it is worth pointing out that if the fluid force is not calculated by the equivalent fluid model but by the fluid solver, the steady-state dynamics and the stability of beam oscillations can also be determined using the methodology given in this work with very low computational costs. In the steady-state cyclic motion, the flexible beam exhibits a coupling phenomenon of multimodal vibration modes, and the fluid-solid coupling mechanism behind it requires further theoretical analysis and experimental verification for a deeper understanding of the nonlinear dynamic behaviour of the underwater flexible beam.

CRediT authorship contribution statement

Jingkun Gao: Writing – original draft, Visualization, Validation, Methodology, Formal analysis, Data curation. **Weidong Zhu:** Writing – review & editing, Methodology, Investigation, Conceptualization. **Yaqing Jin:** Writing – review & editing, Validation,

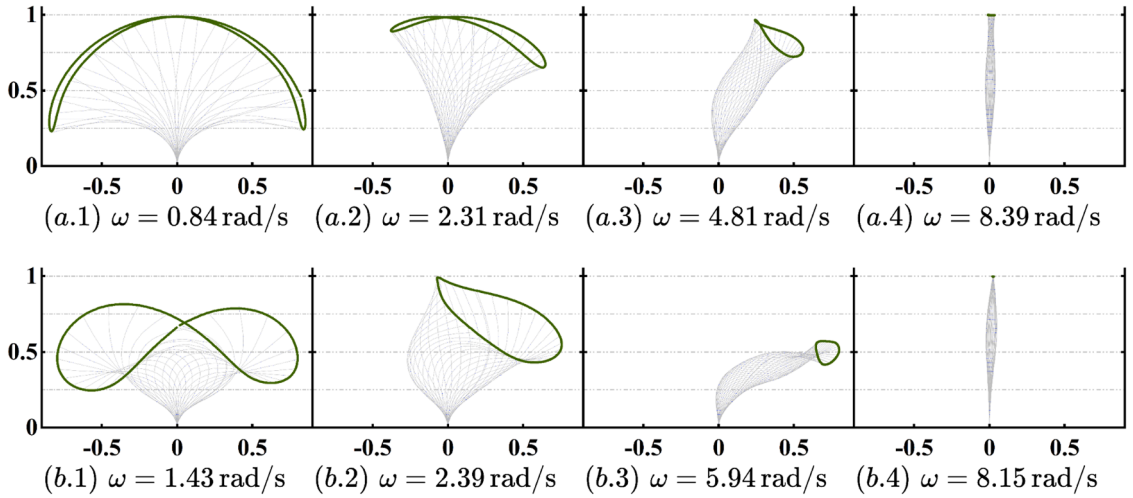

Fig. 10. Snapshots of the motion of the flexible beam for one cycle under different wave period conditions in subplots (a) and (b), which correspond to HDPE and LDPE materials, respectively. The a_w based on $\widehat{\mathbf{U}}_2$ is 35 mm. The coordinate regions represent the OXY plane where the beam is located and the coordinate scale is normalized by the length of the flexible beam. The green curve represents the trajectory of the flexible beam end.

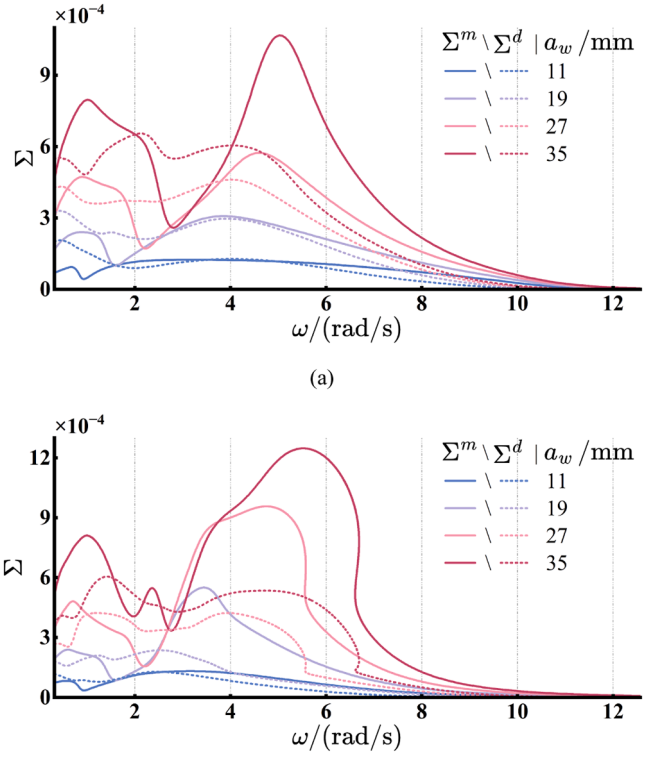

Fig. 11. The force amplitude-frequency characteristic curves of flexible beams under 4 kinds of different flow field conditions based on $\widehat{\mathbf{U}}_2$ are presented in subplots (a) and (b), which correspond to HDPE and LDPE materials, respectively.

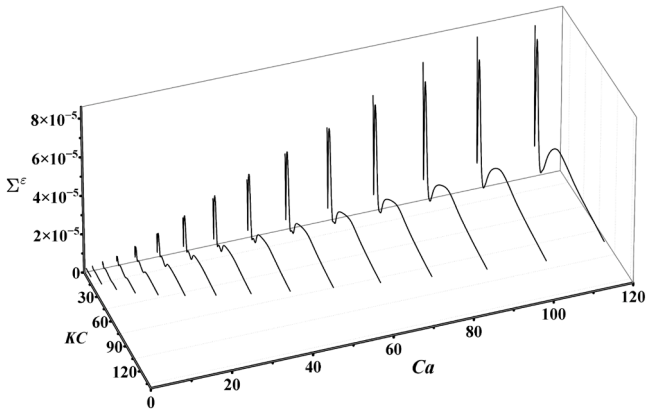

Fig. 12. The variation of ε with KC and Ca based on $\widehat{\mathbf{U}}_1$.

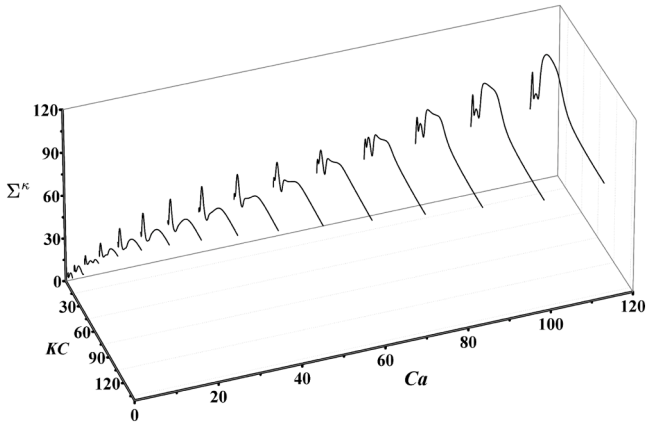

Fig. 13. The variation of κ with KC and Ca based on $\widehat{\mathbf{U}}_1$.

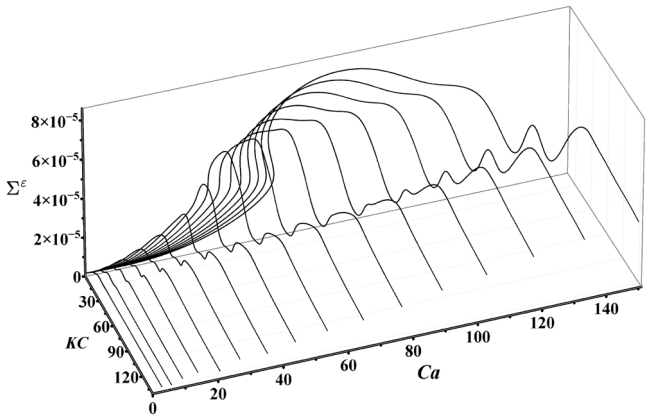

Fig. 14. The variation of ε with KC and Ca based on $\widehat{\mathbf{U}}_2$.

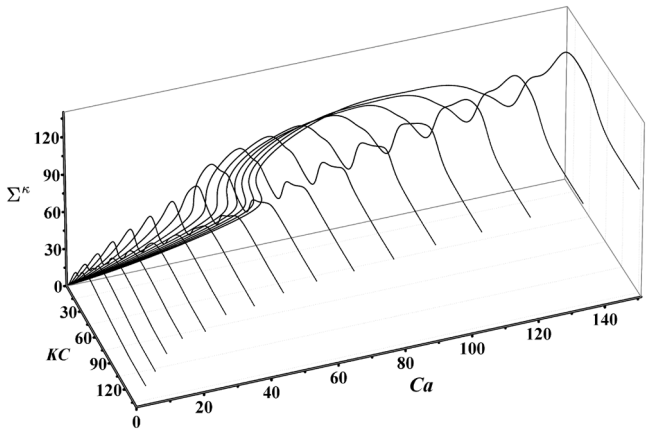

Fig. 15. The variation of κ with KC and Ca based on $\widehat{\mathbf{U}}_2$.

Investigation, Data curation, Conceptualization. **Pengyao Gong:** Writing – review & editing, Investigation, Data curation.

Declaration of competing interest

The authors declare that they have no known competing financial interests or personal relationships that could have appeared to influence the work reported in this paper.

Acknowledgements

This material is partially based upon the work supported by the National Science Foundation under Grant No. 2327916. Any opinions, findings, and conclusions or recommendations expressed in this material are those of the author(s) and do not necessarily reflect the views of the National Science Foundation.

Appendix A

Define $(\bullet)' = \frac{\partial \bullet}{\partial t}$ and $(\bullet)'' = \frac{\partial^2 \bullet}{\partial t^2}$. For the Jacobi matrix of the generalized force vector over $\mathbf{d}^{(n)}$, it can be obtained,

$$\frac{\partial \mathbf{Q}}{\partial \mathbf{d}^{(n)}} = \sum_{i=1}^{N^e} \frac{\partial \mathbf{Q}_F^{e,i}}{\partial \mathbf{d}^{(n)}} - \frac{\partial \mathbf{Q}_I^{e,i}}{\partial \mathbf{d}^{(n)}} - \frac{\partial \mathbf{Q}_E^{e,i}}{\partial \mathbf{d}^{(n)}} \tag{A.1}$$

where,

$$\frac{\partial \mathbf{Q}_F^{e,i}}{\partial \mathbf{d}^{(n)}} = \frac{\partial \mathbf{M}_x^{e,i}}{\partial \mathbf{d}^{(n)}} \cdot F_x^{e,i} + \frac{\partial \mathbf{M}_y^{e,i}}{\partial \mathbf{d}^{(n)}} \cdot F_y^{e,i} + \mathbf{M}_x^{e,i} \cdot \frac{\partial F_x^{e,i}}{\partial \mathbf{d}^{(n)}} + \mathbf{M}_y^{e,i} \cdot \frac{\partial F_y^{e,i}}{\partial \mathbf{d}^{(n)}} \tag{A.2}$$

$$\frac{\partial \mathbf{Q}_I^{e,i}}{\partial \mathbf{d}^{(n)}} = \rho A \begin{pmatrix} \mathrm{I}\left[-2\varepsilon^{e,i'}\varphi^{e,i'}S_\varphi^{e,i} - \left(\varphi^{e,i'}\right)^2 e^{e,i}C_\varphi^{e,i}\right] \frac{\partial \mathbf{M}_x^{e,i}}{\partial \mathbf{d}^{(n)}} \\ +\mathrm{I}\left[2\varepsilon^{e,i'}\varphi^{e,i'}C_\varphi^{e,i} - \left(\varphi^{e,i'}\right)^2 e^{e,i}S_\varphi^{e,i}\right] \frac{\partial \mathbf{M}_y^{e,i}}{\partial \mathbf{d}^{(n)}} \\ +\mathbf{M}_x^{e,i^T} \cdot \mathrm{I}\left[-2\varepsilon^{e,i'}\varphi^{e,i'}C_\varphi^{e,i}\mathbf{N}_2^i - \left(\varphi^{e,i'}\right)^2 \left(C_\varphi^{e,i}\mathbf{N}_1^i - e^{e,i}S_\varphi^{e,i}\mathbf{N}_2^i\right)\right] \\ +\mathbf{M}_y^{e,i^T} \cdot \mathrm{I}\left[-2\varepsilon^{e,i'}\varphi^{e,i'}S_\varphi^{e,i}\mathbf{N}_2^i - \left(\varphi^{e,i'}\right)^2 \left(S_\varphi^{e,i}\mathbf{N}_1^i + e^{e,i}C_\varphi^{e,i}\mathbf{N}_2^i\right)\right] \end{pmatrix} \tag{A.3}$$

$$\frac{\partial \mathbf{Q}_E^{e,i}}{\partial \mathbf{d}^{(n)}} = EA\mathbf{N}_1^{i\,T} \cdot \mathbf{N}_1^i + EI\frac{\partial \mathbf{N}_2^{i\,T}}{\partial \bar{s}} \cdot \frac{\partial \mathbf{N}_2^i}{\partial \bar{s}} \tag{A.4}$$

which

$$\frac{\partial \mathbf{M}_x^{e,i}}{\partial \mathbf{d}^{(n)}} = \mathrm{I}\left[-\left(\mathbf{N}_1^{i\,T} \cdot \mathbf{N}_2^i + \mathbf{N}_2^{i\,T} \cdot \mathbf{N}_1^i\right) S_\varphi^{e,i} - \mathbf{N}_2^{i\,T} \cdot \mathbf{N}_2^i e^{e,i} C_\varphi^{e,i}\right] \tag{A.5}$$

$$\frac{\partial \mathbf{M}_y^{e,i}}{\partial \mathbf{d}^{(n)}} = \mathrm{I}\left[\left(\mathbf{N}_1^{i\,T}\cdot\mathbf{N}_2^i + \mathbf{N}_2^{i\,T}\cdot\mathbf{N}_1^i\right)C_\varphi^{e,i} - \mathbf{N}_2^{i\,T}\cdot\mathbf{N}_2^i e^{e,i} S_\varphi^{e,i}\right] \tag{A.6}$$

For the Jacobi matrix of the generalized force vector over $\dot{\mathbf{d}}^{(n)}$, it can be obtained,

$$\frac{\partial \mathbf{Q}}{\partial \dot{\mathbf{d}}^{(n)}} = \frac{1}{\omega}\sum_{i=1}^{N^e}\frac{\partial \mathbf{Q}_F^{e,i}}{\partial \mathbf{d}^{(n)'}} - \frac{\partial \mathbf{Q}_I^{e,i}}{\partial \mathbf{d}^{(n)'}} - \frac{\partial \mathbf{Q}_C^{i}}{\partial \mathbf{d}^{(n)'}} \tag{A.7}$$

where,

$$\frac{\partial \mathbf{Q}_F^{e,i}}{\partial \mathbf{d}^{(n)'}} = \mathbf{M}_x^{e,i}\cdot\frac{\partial F_x^{e,i}}{\partial \mathbf{d}^{(n)'}} + \mathbf{M}_y^{e,i}\cdot\frac{\partial F_y^{e,i}}{\partial \mathbf{d}^{(n)'}} \tag{A.8}$$

$$\frac{\partial \mathbf{Q}_I^{e,i}}{\partial \mathbf{d}^{(n)'}} = 2\rho A\begin{pmatrix}\mathbf{M}_x^{e,i\,T}\cdot\mathrm{I}\left[-\varphi^{e,i'}S_\varphi^{e,i}\mathbf{N}_1^i - \left(\varepsilon^{e,i'}S_\varphi^{e,i} + \varphi^{e,i'}e^{e,i}C_\varphi^{e,i}\right)\mathbf{N}_2^i\right] \\ +\mathbf{M}_y^{e,i\,T}\cdot\mathrm{I}\left[\varphi^{e,i'}C_\varphi^{e,i}\mathbf{N}_1^i + \left(\varepsilon^{e,i'}C_\varphi^{e,i} - \varphi^{e,i'}e^{e,i}S_\varphi^{e,i}\right)\mathbf{N}_2^i\right]\end{pmatrix} \tag{A.9}$$

$$\frac{\partial \mathbf{Q}_C^{e,i}}{\partial \mathbf{d}^{(n)'}} = \alpha\left(EA\mathbf{N}_1^{i\,T}\cdot\mathbf{N}_1^i + EI\frac{\partial \mathbf{N}_2^{i\,T}}{\partial \bar{s}}\cdot\frac{\partial \mathbf{N}_2^i}{\partial \bar{s}}\right) \tag{A.10}$$

For the Jacobi matrix of the generalized force vector over $\ddot{\mathbf{d}}^{(n)}$, it can be obtained,

$$\frac{\partial \mathbf{Q}}{\partial \ddot{\mathbf{d}}^{(n)}} = \frac{1}{\omega^2}\sum_{k=1}^{N^e}\frac{\partial \mathbf{Q}_F^{e,i}}{\partial \mathbf{d}^{(n)''}} \tag{A.11}$$

Where,

$$\frac{\partial \mathbf{Q}_F^{e,i}}{\partial \mathbf{d}^{(n)''}} = \mathbf{M}_x^{e,i}\cdot\frac{\partial F_x^{e,i}}{\partial \mathbf{d}^{(n)''}} + \mathbf{M}_y^{e,i}\cdot\frac{\partial F_y^{e,i}}{\partial \mathbf{d}^{(n)''}} \tag{A.12}$$

For the Jacobi matrix of the mass matrix over the $(\mathbf{d}^{(n)})_\alpha$, it can be obtained,

$$\begin{aligned}\frac{\partial \mathbf{M}}{\partial (\mathbf{d}^{(n)})_\alpha} &= \sum_{i=1}^{N^e}\frac{\partial \mathbf{M}^{e,i}}{\partial (\mathbf{d}^{(n)})_\alpha} \\ &= \sum_{i=1}^{N^e}\rho A\left(\mathbf{M}_x^{e,i\,T}\cdot\frac{\partial \mathbf{M}_x^{e,i}}{\partial (\mathbf{d}^{(n)})_\alpha} + \frac{\partial \mathbf{M}_x^{e,i\,T}}{\partial (\mathbf{d}^{(n)})_\alpha}\cdot\mathbf{M}_x^{e,i} + \mathbf{M}_y^{e,i\,T}\cdot\frac{\partial \mathbf{M}_y^{e,i}}{\partial (\mathbf{d}^{(n)})_\alpha} + \frac{\partial \mathbf{M}_y^{e,i\,T}}{\partial (\mathbf{d}^{(n)})_\alpha}\cdot\mathbf{M}_y^{e,i}\right)\end{aligned} \tag{A.13}$$

For the Jacobi matrix of the equivalent fluid force vector over the $\mathbf{d}^{(n)}$, it can be obtained,

$$\frac{\partial \mathbf{F}^{e,i}}{\partial \mathbf{d}^{(n)}} = \sum_{i=1}^{N^e}\frac{\partial \mathbf{F}_D^{e,i}}{\partial \mathbf{d}^{(n)}} + \frac{\partial \mathbf{F}_F^{e,i}}{\partial \mathbf{d}^{(n)}} + \frac{\partial \mathbf{F}_{VB}^{e,i}}{\partial \mathbf{d}^{(n)}} + \frac{\partial \mathbf{F}_{AM}^{e,i}}{\partial \mathbf{d}^{(n)}} \tag{A.14}$$

where,

$$\begin{aligned}\frac{\partial \mathbf{F}_D^{e,i}}{\partial \mathbf{d}^{(n)}} &= \rho b C_D\left|U_t^{e,i}\right|\left(\mathbf{T}_t^{e,i}\cdot\left(\mathbf{T}_t^{e,i\,T}\cdot\frac{\partial \widehat{\mathbf{U}}_{rel}^{e,i}}{\partial \mathbf{d}^{(n)}} + \widehat{\mathbf{U}}_{rel}^{e,i\,T}\cdot\frac{\partial \mathbf{T}_t^{e,i}}{\partial \mathbf{d}^{(n)}}\right) + \frac{1}{2}U_t^{e,i}\frac{\partial \mathbf{T}_t^{e,i}}{\partial \mathbf{d}^{(n)}}\right) \\ &= \rho b C_D\left|U_t^{e,i}\right|\left(\mathbf{T}_t^{e,i}\cdot\mathbf{T}_t^{e,i\,T}\cdot\left(\frac{\partial \widehat{\mathbf{U}}^{e,i}}{\partial \mathbf{d}^{(n)}} - \frac{\partial \mathbf{u}^{e,i'}}{\partial \mathbf{d}^{(n)}}\right) + \mathbf{T}_t^{e,i}\cdot\widehat{\mathbf{U}}_{rel}^{e,i\,T}\cdot\mathbf{T}_n^{e,i}\cdot\mathbf{N}_2^i + \frac{1}{2}U_t^{e,i}\mathbf{T}_n^{e,i}\cdot\mathbf{N}_2^i\right)\end{aligned} \tag{A.15}$$

$$\begin{aligned}\frac{\partial \mathbf{F}_F^{e,i}}{\partial \mathbf{d}^{(n)}} &= \rho b C_F\left|U_n^{e,i}\right|\left(\mathbf{T}_n^{e,i}\cdot\left(\mathbf{T}_n^{e,i\,T}\cdot\frac{\partial \widehat{\mathbf{U}}_{rel}^{e,i}}{\partial \mathbf{d}^{(n)}} + \widehat{\mathbf{U}}_{rel}^{e,i\,T}\cdot\frac{\partial \mathbf{T}_n^{e,i}}{\partial \mathbf{d}^{(n)}}\right) + \frac{1}{2}U_n^{e,i}\frac{\partial \mathbf{T}_n^{e,i}}{\partial \mathbf{d}^{(n)}}\right) \\ &= \rho b C_F\left|U_n^{e,i}\right|\left(\mathbf{T}_n^{e,i}\cdot\mathbf{T}_n^{e,i\,T}\cdot\left(\frac{\partial \widehat{\mathbf{U}}^{e,i}}{\partial \mathbf{d}^{(n)}} - \frac{\partial \mathbf{u}^{e,i'}}{\partial \mathbf{d}^{(n)}}\right) - \mathbf{T}_n^{e,i}\cdot\widehat{\mathbf{U}}_{rel}^{e,i\,T}\cdot\mathbf{T}_t^{e,i}\cdot\mathbf{N}_2^i - \frac{1}{2}U_n^{e,i}\mathbf{T}_t^{e,i}\cdot\mathbf{N}_2^i\right)\end{aligned} \tag{A.16}$$

$$\frac{\partial \mathbf{F}_{VB}^{e,i}}{\partial \mathbf{d}^{(n)}} = \rho b h\frac{\partial \widehat{\mathbf{U}}^{e,i}}{\partial \mathbf{d}^{(n)}} \tag{A.17}$$

$$\frac{\partial \mathbf{F}_{AM}^{e,i}}{\partial \mathbf{d}^{(n)}} = \frac{\pi}{4}\rho_f b^2 C_M \left(\frac{\partial \widehat{\mathbf{U}}^{e,i'}}{\partial \mathbf{d}^{(n)}} - \frac{\partial \mathbf{u}^{e,i''}}{\partial \mathbf{d}^{(n)}} \right) \tag{A.18}$$

For the Jacobi matrix of the equivalent fluid force vector over the $\dot{\mathbf{d}}^{(n)}$, it can be obtained,

$$\frac{\partial \mathbf{F}^{e,i}}{\partial \mathbf{d}^{(n)'}} = \sum_{i=1}^{N^e} \frac{\partial \mathbf{F}_D^{e,i}}{\partial \mathbf{d}^{(n)'}} + \frac{\partial \mathbf{F}_F^{e,i}}{\partial \mathbf{d}^{(n)'}} + \frac{\partial \mathbf{F}_{AM}^{e,i}}{\partial \mathbf{d}^{(n)'}} \tag{A.19}$$

where,

$$\frac{\partial \mathbf{F}_D^{e,i}}{\partial \mathbf{d}^{(n)'}} = -\rho b C_D \left| U_t^{e,i} \right| \mathbf{T}_t^{e,i} \cdot \mathbf{T}_t^{e,i^T} \cdot \frac{\partial \mathbf{u}^{e,i'}}{\partial \mathbf{d}^{(n)'}} \tag{A.20}$$

$$\frac{\partial \mathbf{F}_F^{e,i}}{\partial \mathbf{d}^{(n)'}} = -\rho b C_F \left| U_n^{e,i} \right| \mathbf{T}_n^{e,i} \cdot \mathbf{T}_n^{e,i^T} \cdot \frac{\partial \mathbf{u}^{e,i'}}{\partial \mathbf{d}^{(n)'}} \tag{A.21}$$

$$\frac{\partial \mathbf{F}_{AM}^{e,i}}{\partial \mathbf{d}^{(n)'}} = -\frac{\pi}{4}\rho_f b^2 C_M \frac{\partial \mathbf{u}^{e,i''}}{\partial \mathbf{d}^{(n)'}} \tag{A.22}$$

For the Jacobi matrix of the equivalent fluid force vector over the $\ddot{\mathbf{d}}^{(n)}$, it can be obtained,

$$\frac{\partial \mathbf{F}^{e,i}}{\partial \mathbf{d}^{(n)''}} = \sum_{i=1}^{N^e} \frac{\partial \mathbf{F}_{AM}^{e,i}}{\partial \mathbf{d}^{(n)''}} \tag{A.23}$$

where,

$$\frac{\partial \mathbf{F}_{AM}^{e,i}}{\partial \mathbf{d}^{(n)''}} = \frac{\pi}{4}\rho_f b^2 C_M \left(\frac{\partial \widehat{\mathbf{U}}^{e,i'}}{\partial \mathbf{d}^{(n)''}} - \frac{\partial \mathbf{u}^{e,i''}}{\partial \mathbf{d}^{(n)''}} \right) \tag{A.24}$$

There are also some formulas that need to be used in calculations,

$$\frac{\partial \mathbf{u}^{e,i'}}{\partial \mathbf{d}^{(n)}} = \mathrm{I}\left[\begin{pmatrix} -\varepsilon^{e,i'} S_\varphi^{e,i} \mathbf{N}_2^i - \varphi^{e,i'} \left(S_\varphi^{e,i} \mathbf{N}_1^i + e^{e,i} C_\varphi^{e,i} \mathbf{N}_2^i \right) \\ \varepsilon^{e,i'} C_\varphi^{e,i} \mathbf{N}_2^i + \varphi^{e,i'} \left(C_\varphi^{e,i} \mathbf{N}_1^i - e^{e,i} S_\varphi^{e,i} \mathbf{N}_2^i \right) \end{pmatrix} \right] \tag{A.25}$$

$$\frac{\partial \mathbf{u}^{e,i'}}{\partial \mathbf{d}^{(n)'}} = \mathrm{I}\left[\begin{pmatrix} C_\varphi^{e,i} \mathbf{N}_1^i - e^{e,i} S_\varphi^{e,i} \mathbf{N}_2^i \\ S_\varphi^{e,i} \mathbf{N}_1^i + e^{e,i} C_\varphi^{e,i} \mathbf{N}_2^i \end{pmatrix} \right] \tag{A.26}$$

$$\frac{\partial \mathbf{u}^{e,i''}}{\partial \mathbf{d}^{(n)}} = \mathrm{I}\left[\begin{pmatrix} -\varepsilon^{e,i''} S_\varphi^{e,i} \mathbf{N}_2^i - \varphi^{e,i''} \left(S_\varphi^{e,i} \mathbf{N}_1^i + e^{e,i} C_\varphi^{e,i} \mathbf{N}_2^i \right) - 2\varepsilon^{e,i'} \varphi^{e,i'} C_\varphi^{e,i} \mathbf{N}_2^i - \left(\varphi^{e,i'} \right)^2 \left(C_\varphi^{e,i} \mathbf{N}_1^i - e^{e,i} S_\varphi^{e,i} \mathbf{N}_2^i \right) \\ \varepsilon^{e,i''} C_\varphi^{e,i} \mathbf{N}_2^i + \varphi^{e,i''} \left(C_\varphi^{e,i} \mathbf{N}_1^i - e^{e,i} S_\varphi^{e,i} \mathbf{N}_2^i \right) - 2\varepsilon^{e,i'} \varphi^{e,i'} S_\varphi^{e,i} \mathbf{N}_2^i - \left(\varphi^{e,i'} \right)^2 \left(S_\varphi^{e,i} \mathbf{N}_1^i + e^{e,i} C_\varphi^{e,i} \mathbf{N}_2^i \right) \end{pmatrix} \right] \tag{A.27}$$

$$\frac{\partial \mathbf{u}^{e,i''}}{\partial \mathbf{d}^{(n)'}} = 2\mathrm{I}\left[\begin{pmatrix} -\varepsilon^{e,i'} S_\varphi^{e,i} \mathbf{N}_2^i - \varphi^{e,i'} \left(S_\varphi^{e,i} \mathbf{N}_1^i + e^{e,i} C_\varphi^{e,i} \mathbf{N}_2^i \right) \\ \varepsilon^{e,i'} C_\varphi^{e,i} \mathbf{N}_2^i + \varphi^{e,i'} \left(C_\varphi^{e,i} \mathbf{N}_1^i - e^{e,i} S_\varphi^{e,i} \mathbf{N}_2^i \right) \end{pmatrix} \right] \tag{A.28}$$

$$\frac{\partial \mathbf{u}^{e,i''}}{\partial \mathbf{d}^{(n)''}} = \mathrm{I}\left[\begin{pmatrix} C_\varphi^{e,i} \mathbf{N}_1^i - e^{e,i} S_\varphi^{e,i} \mathbf{N}_2^i \\ S_\varphi^{e,i} \mathbf{N}_1^i + e^{e,i} C_\varphi^{e,i} \mathbf{N}_2^i \end{pmatrix} \right] \tag{A.29}$$

Data availability

Data will be made available on request.

References

Aju, E.J., Gong, P., Pham, D.T., Kaushik, K., Jin, Y., 2022. On the wake dynamics and thrust generation of a foil flapping over solid and sedimentary beds. Exp. Fluids. https://doi.org/10.1007/s00348-022-03386-w.

Akcabay, D.T., Young, Y.L., 2012. Hydroelastic response and energy harvesting potential of flexible piezoelectric beams in viscous flow. Physics of Fluids 24, 054106. https://doi.org/10.1063/1.4719704.
Batchelor, G.K., 1999. An Introduction to Fluid Dynamics. Cambridge University Press, New York.
Beth Schaefer, R., Nepf, H., 2022. Wave damping by seagrass meadows in combined wave-current conditions. Limnol. Oceanogr. https://doi.org/10.1002/lno.12102.
Cavallaro, L., Viviano, A., Paratore, G., Foti, E., 2018. Experiments on surface waves interacting with flexible aquatic vegetation. Ocean Science Journal. https://doi.org/10.1007/s12601-018-0037-8.
Chatterjee, R., Shah, C.L., Gupta, S., Sarkar, S., 2024. Energy harvesting in a flow-induced vibrating flapper with biomimetic gaits. Int. J. Mech. Sci. 272, 109150. https://doi.org/10.1016/j.ijmecsci.2024.109150.
Chen, Z., Liu, Y., Sung, H.J., 2024. Snap-through dynamics of buckled flexible filaments in a side-by-side configuration. Int. J. Heat. Fluid. Flow. 107, 109417. https://doi.org/10.1016/j.ijheatfluidflow.2024.109417.
Cheung, Y.K., Chen, S.H., Lau, S.L., 1990. Application of the incremental harmonic balance method to cubic non-linearity systems. J. Sound. Vib. 140, 273–286. https://doi.org/10.1016/0022-460X(90)90528-8.
Dean, R.G., Dalrymple, R.A., 1991. Water Wave Mechanics For Engineers and Scientists. world scientific publishing company.
Dehrouyeh-Semnani, A.M., 2025. Geometrically exact post-buckling and post-flutter of standing cantilevered pipe conveying fluid. Physica D: Nonlinear Phenomena 472, 134478. https://doi.org/10.1016/j.physd.2024.134478.
de Langre, E., 2019. Plant vibrations at all scales: a review. J. Exp. Bot. https://doi.org/10.1093/jxb/erz209.
Denny, M., Gaylord, B., Helmuth, B., Daniel, T., 1998. The menace of momentum: dynamic forces on flexible organisms. Limnol. Oceanogr. 43, 955–968. https://doi.org/10.4319/lo.1998.43.5.0955.
Divyaprakash, Garg, M., Kumar, A., Bhattacharya, A., 2024. A review of computational modeling of fluid-immersed flexible Filaments. J. Indian Inst. Sci. 104, 277–301. https://doi.org/10.1007/s41745-024-00423-x.
Farokhi, H., Tavallaeinejad, M., Païdoussis, M.P., 2021. Geometrically exact dynamics of cantilevered pipes conveying fluid. J. Fluids. Struct. 106, 103364. https://doi.org/10.1016/j.jfluidstructs.2021.103364.
Glantz, S., Slinker, B., Neilands, T., 2016. Primer of Applied Regression & Analysis of Variance, 3rd edition. McGraw Hill /Medical, New York. Third Edition.
Guo, Y., Zhu, B., Li, J., Li, Y., 2024. Nonlinear geometrically exact dynamics of hyperelastic pipes conveying fluid: comparative study of different hyperelastic models. Thin-Walled Structures 205, 112526. https://doi.org/10.1016/j.tws.2024.112526.
Hall, K.C., Ekici, K., Thomas, J.P., Dowell, E.H., 2013. Harmonic balance methods applied to computational fluid dynamics problems. Int. J. Comut. Fluid. Dyn. https://doi.org/10.1080/10618562.2012.742512.
Hasan, Md.S., Hoskoti, L., Deepu, P., M. Sucheendran, M., 2023. Nonlinear oscillations of a flexible fiber under gravity waves. European Physical Journal-Special Topics. https://doi.org/10.1140/epjs/s11734-022-00663-x.
Henderson, S.M., 2019. Motion of buoyant, flexible aquatic vegetation under waves: simple theoretical models and parameterization of wave dissipation. Coast. Eng. 152, 103497. https://doi.org/10.1016/j.coastaleng.2019.04.009.
Huang, W.-X., Shin, S.J., Sung, H.J., 2007. Simulation of flexible filaments in a uniform flow by the immersed boundary method. J. Comput. Phys. 226, 2206–2228. https://doi.org/10.1016/j.jcp.2007.07.002.
Jacobsen, N.G., Bakker, W., Uijttewaal, W.S.J., Uittenbogaard, R., 2019. Experimental investigation of the wave-induced motion of and force distribution along a flexible stem. J. Fluid. Mech. https://doi.org/10.1017/jfm.2019.739.
Jin, C., Zhang, J., 2022. Numerical investigation of the wave interaction with flexible vegetation: model setup and validation for a single stem study case. Anthropocene Coasts. https://doi.org/10.1007/s44218-022-00003-5.
Ju, R., Fan, W., Zhu, W., 2020. An efficient galerkin averaging-incremental harmonic balance method based on the fast fourier transform and tensor contraction. Journal of Vibration and Acoustics-Transactions of The Asme. https://doi.org/10.1115/1.4047235.
Keulegan, G., Carpenter, L., 1958. Forces on cylinders and plates in an oscillating fluid. J. Res. Natl. Bur Stand. (1934). https://doi.org/10.6028/jres.060.043.
Kumar, K., Kumar, V., Deepu, P., Ramya, P., 2021. Oscillations of a flexible filament under surface gravity waves. Phys. Rev. Fluids. https://doi.org/10.1103/PhysRevFluids.6.114004.
LaBryer, A., Attar, P.J., 2010. A harmonic balance approach for large-scale problems in nonlinear structural dynamics. Comput. Struct. https://doi.org/10.1016/j.compstruc.2010.06.003.
Leclercq, T., de Langre, E., 2018. Reconfiguration of elastic blades in oscillatory flow. J. Fluid. Mech. https://doi.org/10.1017/jfm.2017.910.
Lei, J., Nepf, H., 2019a. Wave damping by flexible vegetation: connecting individual blade dynamics to the meadow scale. Coast. Eng. https://doi.org/10.1016/j.coastaleng.2019.01.008.
Lei, J., Nepf, H., 2019b. Blade dynamics in combined waves and current. J. Fluids. Struct. https://doi.org/10.1016/j.jfluidstructs.2019.03.020.
Li, G., Chen, X., Zhou, F., Liang, Y., Xiao, Y., Cao, X., Zhang, Z., Zhang, M., Wu, B., Yin, S., Xu, Y., Fan, H., Chen, Z., Song, W., Yang, Wenjing, Pan, B., Hou, J., Zou, W., He, S., Yang, X., Mao, G., Jia, Z., Zhou, H., Li, T., Qu, S., Xu, Z., Huang, Z., Luo, Y., Xie, T., Gu, J., Zhu, S., Yang, Wei, 2021. Self-powered soft robot in the Mariana Trench. Nature. https://doi.org/10.1038/s41586-020-03153-z.
Li, L., Zhu, W.D., Zhang, D.G., Du, C.F., 2015. A new dynamic model of a planar rotating hub–beam system based on a description using the slope angle and stretch strain of the beam. J. Sound. Vib. 345, 214–232. https://doi.org/10.1016/j.jsv.2015.01.009.
Li, Y., Wang, H., Li, X., Wang, Y., Lu, S., Tang, Q., Luo, J., Yang, P., 2024. Recent progress in soft robots: principles, designs, and applications. SMART MATERIALS AND STRUCTURES 33. https://doi.org/10.1088/1361-665X/ad8053.
Luhar, M., Nepf, H.M., 2011. Flow-induced reconfiguration of buoyant and flexible aquatic vegetation. Limnol. Oceanogr. https://doi.org/10.4319/lo.2011.56.6.2003.
Luhar, M., Nepf, H.M., 2016. Wave-induced dynamics of flexible blades. J. Fluids. Struct. https://doi.org/10.1016/j.jfluidstructs.2015.11.007.
Marjoribanks, T.I., Paul, M., 2022. Modelling flow-induced reconfiguration of variable rigidity aquatic vegetation. Journal of Hydraulic Research. https://doi.org/10.1080/00221686.2020.1866693.
Mazharmanesh, S., Young, J., Tian, F.-B., Ravi, S., Lai, J.C.S., 2022. Energy harvesting of inverted piezoelectric flags in an oscillating flow. J. Fluids. Struct. 115, 103762. https://doi.org/10.1016/j.jfluidstructs.2022.103762.
Meirovitch, L., 2010. Fundamentals of Vibrations. Waveland Press.
Mullarney, J.C., Henderson, S.M., 2010. Wave-forced motion of submerged single-stem vegetation. Journal of Geophysical Research-Oceans. https://doi.org/10.1029/2010JC006448.
Poi, A.S.G., Gallardo, L.I., Casco, S.L., Sabater, L.M., Úbeda, B., 2021. Influence of macrophyte complexity and environmental variables on macroinvertebrate assemblages across a subtropical wetland system. Wetlands 41, 105. https://doi.org/10.1007/s13157-021-01508-4.
Reis, R.A., Fortes, C.J.E.M., Rodrigues, J.A., Hu, Z., Suzuki, T., 2024. Experimental study on drag coefficient of flexible vegetation under non-breaking waves. Ocean Engineering. https://doi.org/10.1016/j.oceaneng.2024.117002.
Ri, K., Han, P., Kim, I., Kim, W., Cha, H., 2020. Nonlinear forced vibration analysis of composite beam combined with DQFEM and IHB. AIP. Adv. 10, 085112. https://doi.org/10.1063/5.0015053.
Suresh, D.B., Aju, E.J., Pham, D.T., Jin, Y., 2021. On the incipient sediment suspension downstream of three-dimensional wall-mounted obstacles. Physics of Fluids. https://doi.org/10.1063/5.0059969.
Vogel, S., 1984. Drag and flexibility in sessile organisms. Am. Zool. 24, 37–44.
Vymazal, J., 2013. Emergent plants used in free water surface constructed wetlands: a review. Ecological Engineering, Plants in constructed, restored and created wetlands 61, 582–592. https://doi.org/10.1016/j.ecoleng.2013.06.023.
Wang, C., Tang, H., Zhang, X., 2022. Fluid-structure interaction of bio-inspired flexible slender structures: a review of selected topics. Bioinspir. Biomim. https://doi.org/10.1088/1748-3190/ac68ba.

Wei, Z., Shao, Y., Kristiansen, T., Kristiansen, D., 2024. An efficient numerical solver for highly compliant slender structures in waves: application to marine vegetation. J. Fluids. Struct. https://doi.org/10.1016/j.jfluidstructs.2024.104170.

Woiwode, L., Balaji, N.N., Kappauf, J., Tubita, F., Guillot, L., Vergez, C., Cochelin, B., Grolet, A., Krack, M., 2020. Comparison of two algorithms for harmonic balance and path continuation. Mech. Syst. Signal. Process. https://doi.org/10.1016/j.ymssp.2019.106503.

Xia, Q., Li, H., Song, N., Wu, Z., Wang, X., Sun, X., Zhang, S., Yang, C., 2023. Research on flexible collapsible fluid-driven bionic robotic fish. Ocean Engineering 276, 114203. https://doi.org/10.1016/j.oceaneng.2023.114203.

Yan, Z., Dai, H., Wang, Q., Atluri, S.N., 2023. Harmonic balance methods: a review and recent developments. Computer Modeling In Engineering & Sciences. https://doi.org/10.32604/cmes.2023.028198.

Yin, K., Lin, M., Xu, S., Hao, J., Mao, L., Li, M., 2023a. Numerical investigation of submerged flexible vegetation dynamics and wave attenuation under combined waves and following currents. Ocean Engineering. https://doi.org/10.1016/j.oceaneng.2023.114437.

Yin, K., Xu, S., Huang, W., Lin, M., 2023b. Experimental and numerical investigation of wave-induced dynamics of emergent flexible vegetation. Ocean Engineering 289, 116155. https://doi.org/10.1016/j.oceaneng.2023.116155.

Zeller, R.B., Weitzman, J.S., Abbett, M.E., Zarama, F.J., Fringer, O.B., Koseff, J.R., 2014. Improved parameterization of seagrass blade dynamics and wave attenuation based on numerical and laboratory experiments. Limnol. Oceanogr. https://doi.org/10.4319/lo.2014.59.1.0251.

Zhang, J., Nakamura, T., 2024. Dynamics of a wall-mounted flexible plate in oscillatory flows. Physics of Fluids. https://doi.org/10.1063/5.0214147.

Zhang, X., Nepf, H., 2021. Wave-induced reconfiguration of and drag on marsh plants. J. Fluids. Struct. https://doi.org/10.1016/j.jfluidstructs.2020.103192.

Zhu, L., Zou, Q.P., Huguenard, K., Fredriksson, D.W., 2020. Mechanisms for the asymmetric motion of submerged aquatic vegetation in waves: a consistent-mass cable model. Journal of Geophysical Research-Oceans. https://doi.org/10.1029/2019JC015517.